Molecular Mechanism for Attractant Signaling to DHMA by *E. coli* Tsr

Asuka A. Orr,[1] Jingyun Yang,[1] Nitesh Sule,[1] Ravi Chawla,[1] Kenneth G. Hull,[2] Mingzhao Zhu,[2] Daniel Romo,[2] Pushkar P. Lele,[1] Arul Jayaraman,[1] Michael D. Manson,[3,*] and Phanourios Tamamis[1,*]

[1]Artie McFerrin Department of Chemical Engineering, Texas A&M University, College Station, Texas; [2]Department of Chemistry & Biochemistry and CPRIT Synthesis and Drug-Lead Discovery Laboratory, Baylor University, Waco, Texas; and [3]Department of Biology, Texas A&M University, College Station, Texas

ABSTRACT   The attractant chemotaxis response of *Escherichia coli* to norepinephrine requires that it be converted to 3,4-di-hydroxymandelic acid (DHMA) by the monoamine oxidase TynA and the aromatic aldehyde dehydrogenase FeaB. DHMA is sensed by the serine chemoreceptor Tsr, and the attractant response requires that at least one subunit of the periplasmic domain of the Tsr homodimer (pTsr) has an intact serine-binding site. DHMA that is generated in vivo by *E. coli* is expected to be a racemic mixture of the (*R*) and (*S*) enantiomers, so it has been unclear whether one or both chiral forms are active. Here, we used a combination of state-of-the-art tools in molecular docking and simulations, including an in-house simulation-based docking protocol, to investigate the binding properties of (*R*)-DHMA and (*S*)-DHMA to *E. coli* pTsr. Our studies computationally predicted that (*R*)-DHMA should promote a stronger attractant response than (*S*)-DHMA because of a consistently greater-magnitude piston-like pushdown of the pTsr α-helix 4 toward the membrane upon binding of (*R*)-DHMA than upon binding of (*S*)-DHMA. This displacement is caused primarily by interaction of DHMA with Tsr residue Thr156, which has been shown by genetic studies to be critical for the attractant response to *L*-serine and DHMA. These findings led us to separate the two chiral species and test their effectiveness as chemoattractants. Both the tethered cell and motility migration coefficient assays validated the prediction that (*R*)-DHMA is a stronger attractant than (*S*)-DHMA. Our study demonstrates that refined computational docking and simulation studies combined with experiments can be used to investigate situations in which subtle differences between ligands may lead to diverse chemotactic responses.

SIGNIFICANCE   3,4-Dihydroxymandelic acid (DHMA) is a Tsr chemoattractant that binds to the periplasmic domain of the *E. coli* Tsr chemoreceptor (pTsr). DHMA produced in *E. coli* is presumably a racemic mixture of its two enantiomers, (*R*)-DHMA and (*S*)-DHMA. We used a combination of computational studies, primarily based on docking and molecular dynamics simulations, to predict that the two enantiomers will bind in different orientations and interact differently with key pTsr residues. The binding of (*R*)-DHMA is predicted to cause a greater downward piston-like movement of α-helix 4 of pTsr than binding of (*S*)-DHMA. Experiments demonstrated that (*R*)-DHMA and (*S*)-DHMA are both attractants, with (*R*)-DHMA being more potent than (*S*)-DHMA. This result validates our approach of making computational predictions to guide experimental design.

INTRODUCTION

It has recently become clear that chemotaxis in *E. coli* confers advantages other than the ability to migrate to higher concentrations of nutrients. Signaling molecules derived both from other microorganisms and from the host have been identified as potent attractants. Most notable in the first group is the general quorum-sensing signal AI-2, used to assess bacterial population density (1). It is sensed by a compound chemoreceptor (2) that involves the periplasmic AI-2-binding protein LsrB (3) and the membrane-associated methyl-accepting chemotaxis protein Tsr, which was originally annotated as the serine chemoreceptor (4). Chemotaxis to AI-2 has been shown to be important in the initiation of the cell aggregation that leads to biofilm development (5,6).

Included in the second group is the host neurotransmitter and adrenal hormone norepinephrine (NE), also sensed by Tsr (7). NE is converted to the actual attractant, 3,4-dihydroxymandelic acid (DHMA), by the action of two bacterial enzymes, the periplasmic monoamine oxidase TynA and the

cytoplasmic aromatic aldehyde dehydrogenase FeaB (8). DHMA is sensed by binding to the periplasmic domain of Tsr (pTsr). Therefore, chemotaxis to NE requires that 3,4-dihydroxyphenyl-glycol-aldehyde (DOPEGAL) be formed by deamination of NE in the periplasm; that DOPEGAL be imported into the cytoplasm, where it is converted to DHMA; and that DHMA then be exported out to the periplasm (7,9) (Fig. 1). This scenario should mean that DHMA will be effective as a chemoattractant at much lower concentrations than NE, which is the case.

DHMA also shares with NE the capability of inducing virulence genes contained in enterohemorrhagic *E. coli* (10). A number of other host-produced compounds also are active as either chemoattractants or repellents (11). NE is released in copious amounts in the gastrointestinal tract, with high concentrations found in gut-associated lymphoid tissue (12). The presence of detectable amounts of DHMA in the mouse gastrointestinal tract, however, requires the presence of the resident microbiota, as DHMA is not found in the feces or cecal contents of germ-free mice (10).

Our initial studies showed that DHMA is active as an attractant at very low concentrations but has the perplexing property of losing its activity at concentrations of 500 μM and above (7). DHMA interacts with the periplasmic serine-binding site of Tsr. A Tsr dimer having only one intact serine-binding site detects DHMA as an attractant as well as a fully intact dimer. However, the loss of attraction at high concentrations depends on having both serine-binding sites of the Tsr dimer intact. This result suggests that the attractant response is abrogated when both binding sites are occupied with DHMA.

DHMA is commercially available only as a racemic mixture of its two enantiomers (*R*)-DHMA and (*S*)-DHMA. The DHMA produced by *E. coli* is probably also a racemic mixture (Fig. 1). To determine whether one or both enantiomers of DHMA are active as attractants, we used computational docking and simulation-based approaches to study the binding of (*R*)- and (*S*)-DHMA to pTsr. Previous experimental (13) and computational (14) studies indicated that the binding of chemoattractants to Tsr or Tar results in a downward (toward-the-membrane) piston-like movement of α-helix 4 of the periplasmic domain. To study the effect of subtle physicochemical differences of the two chiral forms of DHMA on their interactions with pTsr, and to determine whether any binding differences between the two could result in potential structural and allosteric conformational differences linked to chemotaxis, we used highly accurate docking methods complemented with multiple, multi-nanosecond (multi-ns) simulations. First, we used an in-house computational protocol (15–20) to investigate both enantiomers of DHMA binding to pTsr after an initial computational study focused on (*R*)-DHMA docking to pTsr (15). This method allows for nearly exhaustive docking of a compound in a receptor binding pocket, with the most energetically favorable binding mode (i.e., the one the lowest in binding energy) being revealed through molecular dynamics (MD) simulations and physics-based energy calculations (15–20). Since its development, the method has been used to investigate several other ligand-protein complexes (16–20). Subsequently, we employed multiple multi-ns MD simulations to investigate the most energetically favorable binding modes of (*R*)- and (*S*)-DHMA in complex with pTsr. We focused our analysis on the interactions between the key residues of the protein with the two compounds, focusing on potential conformational changes induced by their binding.

MATERIALS AND METHODS

Computational methods

We performed multi-ns, explicit-solvent MD simulations followed by structural, conformational, and energetic analyses to compare the binding properties of (*R*)- and (*S*)-DHMA complexed with *E. coli* pTsr. The starting structure for the MD simulations corresponded to the most energetically favorable binding mode of each enantiomer in complex with pTsr, determined independently using a docking-refinement protocol developed in house (15–20). All analyses were performed using CHARMM (21), Wordom (22), and in-house FORTRAN programs.

Docking (S)-DHMA bound to pTsr

We used our in-house docking-refinement protocol to derive the most energetically favorable binding modes of (*R*)- and (*S*)-DHMA in complex with *E. coli* pTsr (15–20). Specifically, the (*R*)-DHMA-pTsr complex structure was derived in our recent previous study (15), and the (*S*)-DHMA-pTsr complex structure was derived in the current study. The docking-refinement protocol (15–20) can be divided into the following stages: 1) initial positioning of the ligand within the receptor binding pocket, based on available experimental data; 2) multiple short MD docking simulations of the ligand within the receptor binding pocket, with the ligand forced to rotate and sample different binding modes while being constrained in the pocket by
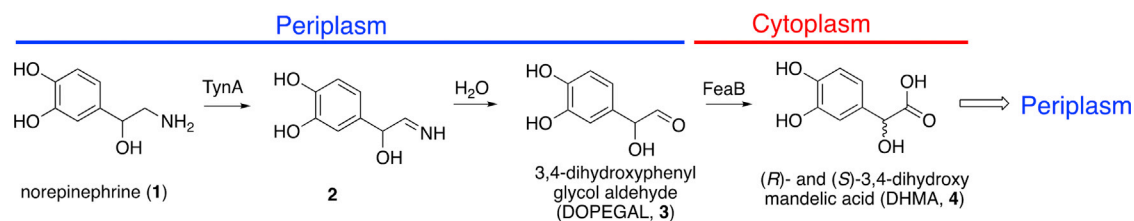

FIGURE 1 Reaction schematic of the conversion of NE to DHMA. NE is converted by the periplasmic monoamine oxidase TynA into DOPEGAL, and DOPEGAL is converted by the cytoplasmic aromatic aldehyde dehydrogenase FeaB into (*R*)- or (*S*)-DHMA. To see this figure in color, go online.

harmonic and quartic spherical potentials and with the absence of any constraints on the binding-pocket residues; 3) interaction-energy calculations to select the most probable binding modes generated by the short docking simulations; and 4) multiple explicit-solvent MD simulations and physical-chemistry-based free energy calculations to identify the most favorable binding mode of the ligand-receptor complex (Fig. S1). The independent use of harmonic and quartic harmonic potential functions that constrain the ligand in the binding pocket with respect to its initial position encourage the exploration of binding modes both away from (quartic) and proximal to (harmonic) their initial positioning.

In this study, we docked (*S*)-DHMA in the serine-binding site of the experimentally resolved crystal structure of the serine-pTsr complex (Protein Data Bank, PDB: 3ATP (13)) using the same parameters as in our previous study of (*R*)-DHMA binding to pTsr (15). Details about the docking of (*S*)-DHMA are described in Supporting Material. From the short MD docking simulations, we collected 15 binding modes of the (*S*)-DHMA-pTsr complex. All 15 binding modes were investigated using 20-ns MD simulations, and the binding mode resulting in the most energetically favorable complex, as assessed by MM-GBSA association free energy calculations (23), was selected. We verified that all the other binding modes of the (*S*)-DHMA-pTsr complex were far less energetically favorable than the identified binding mode, and the identified binding mode was selected for further investigation. In the case of (*R*)-DHMA, the two most energetically favorable binding modes were similar in energy and also similar in structure (15); thus, we selected the binding mode resulting in the most favorable association free energy for further investigation. The selected binding modes of (*S*)-DHMA, derived in the current study, and (*R*)-DHMA, derived in our previous study (15), in complex with pTsr were used as initial structures in five replicate 100-ns MD simulations.

Investigating (R)-DHMA and (S)-DHMA in complex with pTsr using multiple MD simulations

Using the structures of the most energetically favorable binding modes as initial structures, we performed five independent 100-ns MD simulations of bound (*R*)- and (*S*)-DHMA. MD simulations refined intermolecular interactions and the complex structures for detailed examination of the key interactions between the enantiomers and pTsr. They also facilitated the investigation of the conformational properties of the pTsr protein, including allosteric effects, induced by the binding of the enantiomers. A short, 2-ns equilibration stage was introduced before each simulation. Subsequently, five 100-ns MD simulations were performed for each system, resulting in an aggregate duration of 0.5 μs per system. Multiple multi-ns MD simulations of the ligand-binding domain, as performed in (14), were preferred over longer coarse-grained simulations or shorter all-atom simulations of the entire Tsr protein bound to the enantiomers. The former lacks detail in the ligand-binding site, whereas the latter prevents reaching equilibrium in piston-like motions. Our simulated system provided a suitable balance between atomic details of the key interactions of pTsr with the two enantiomers and the observation of allosteric effects associated with attractant signaling (14). All MD simulations were performed using explicit water with periodic boundary conditions. Additional information on setup and parameters is detailed in (15) and in Supporting Material. Coordinates of (*R*)- and (*S*)-DHMA in complex with pTsr from the 100-ns MD simulations are provided (Data S1).

We performed root mean-squared deviation (RMSD) calculations of the ligand heavy atoms with respect to 1) the initial position of the ligand for each independent trajectory 2), the average ligand structure for each independent trajectory, and 3) the average ligand structure from the combined five replicate trajectories. The RMSD calculations were used to determine 1) whether the initial structure identified by our docking-refinement protocol was conserved in all multi-ns MD simulations, 2) whether the orientation of both ligands was stable within their respective simulations, and 3) whether the orientation of both ligands was reproduced in all five simulations. Before the RMSD calculations, the trajectories were aligned with the pTsr backbone atoms of both subunits.

We also identified key interactions associated with the binding of (*R*)- and (*S*)-DHMA through per-residue interaction free energy calculations, analogously to (16,17,19,20,24–28). This analysis complemented an examination of hydrogen bonds, ligand-protein contacts, and water-mediated interactions within the complex. This approach provided insights into the interplay of the interactions with the structure of the (*R*)- and (*S*)-DHMA-pTsr complexes. The analysis was performed to examine, and potentially differentiate, key interactions between the two enantiomers and pTsr. The determination of water-mediated interactions and per-residue interaction free energy calculations is described briefly in Supporting Material and described in detail in (16,17,19,20).

Investigating piston-like motions in pTsr caused by binding of (R)-DHMA and (S)-DHMA

According to the x-ray studies of Tajima et al. (13), binding of *L*-serine to *E. coli* pTsr induces a conformational change in residues 158–172 of α-helix 4 (13). This helix is contiguous with the second transmembrane helix, which connects the periplasmic domain of Tsr to the cytoplasmic HAMP domain (29,30). To investigate the conformational dynamics within pTsr, we analyzed the dynamics of α-helix 4 residues 158–172 throughout the multiple multi-ns MD simulations using calculations quantifying the motions of these residues. Based on the quantified motions of α-helix 4 residues, we defined a metric to compare the potential signaling strength of (*R*)- and (*S*)-DHMA as described below.

We calculated the deviation between the position of α-helix 4 in each simulation snapshot and its position in the crystal structure of the unbound pTsr (extracted from PDB: 2D4U (13)) and compared it with the deviation in the crystal structure of serine-bound pTsr (PDB: 3ATP (13)). Before our analysis, the simulation snapshots of all simulated systems and the crystal structure of serine in complex with pTsr were aligned with the crystal structure of apo pTsr using all Cα atoms. To describe the position of the helix within a structure, we calculated the geometric center of the Cα atoms of residues 158–172 of the signaling subunit. As a point of reference, we calculated the vector of the Cα geometric center of the experimentally resolved apo pTsr to the Cα geometric center of the experimentally resolved serine-bound pTsr. This vector was used as a baseline for Eqs. 1 and 2. We defined a metric to evaluate the signaling strength of (*R*)- and (*S*)-DHMA based on the deviations projected onto the baseline vectors or the projected lengths. The vectors used to describe the position of the helix are shown in Fig. 2.

$$\cos(\theta_i) = \frac{\lambda^2_{3ATP-2D4U} + \lambda^2_{i-2D4U} - \lambda^2_{i-3ATP}}{2\lambda_{3ATP-2D4U}\,\lambda_{i-2D4U}} \quad (1)$$

$$p_i = \frac{\cos(\theta_i)\,\lambda_{i-2D4U}}{\lambda_{3ATP-2D4U}} \quad (2)$$

According to our definition, Eq. 1 isolates the direction of motion in α-helix 4 of the ligand-pTsr complex that is likely to contribute to pTsr signaling. Equation 2 provides the magnitude of the motion of α-helix 4 in the direction of interest, defined by Eq. 1, normalized by the change in position observed in the crystal structures of the unbound and serine-bound pTsr. In Eq. 1, the angle between the vector of the helix in the crystal structure of serine-bound pTsr to the crystal structure in apo pTsr, and the vector of the helix in a simulation snapshot of pTsr bound to (*R*)- or (*S*)-DHMA and the crystal structure of apo pTsr, θ_i, is determined through the law of cosines. λ corresponds to the length between the helix in the crystal structure of the serine-bound pTsr and the crystal structure of the apo pTsr (3ATP-2D4U), the helix in a simulation snapshot of pTsr bound to (*R*)- or (*S*)-DHMA and the crystal structure of apo pTsr (*i*-2D4U), or the helix in a simulation snapshot of pTsr bound to (*R*)- or (*S*)-DHMA and the crystal structure of the serine-bound pTsr (*i*-3ATP). In Eq. 2, the length between the helix in a simulation snapshot of pTsr bound to (*R*)- or (*S*)-DHMA
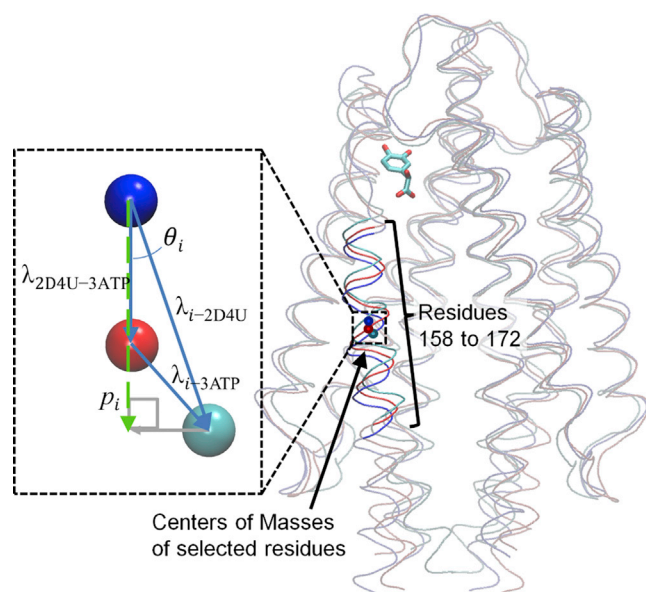
FIGURE 2 Schematic of the vectors used to calculate the projected lengths. Tsr is shown in a gray tube representation. Residues 158–172 of the crystal structure of apo and serine-bound pTsr are shown in blue and red tube representations. Residues 158–172 of the simulated snapshot of pTsr bound to (*R*)-DHMA or (*S*)-DHMA are shown in a cyan tube representation. The geometric centers of residues 158–172 are shown as blue, red, and cyan spheres in the crystal structure of apo pTsr, the crystal structure of serine-bound pTsr, and the simulated snapshot of pTsr bound to (*R*)-DHMA or (*S*)-DHMA, respectively. In the zoomed-in window, vectors between the centers of mass are indicated by blue arrows. The projection of the vector $\lambda_{i\text{-}2D4U}$ onto the baseline vector, $\lambda_{2D4U\text{-}3ATP}$, is indicated by a gray arrow. The resulting projected length, p_i, which is shown as a dashed green arrow. To see this figure in color, go online.

and the crystal structure of apo pTsr ($\lambda_{i\text{-}2D4U}$) is projected onto the baseline vector and normalized using the length between the helix in the crystal structure of serine-bound pTsr and the crystal structure of the apo pTsr ($\lambda_{3ATP\text{-}2D4U}$) to give the reported projected length, p_i. According to the defined metric, a p_i value of 1 indicates a movement of α-helix 4 in response to binding of DHMA comparable to the movement induced by serine, a value > -1 indicates a movement of α-helix 4 greater than the movement induced by serine, and a value < -1 indicates a movement of α-helix 4 less than the movement induced by serine. The vectors used to describe the position of the helix are shown in Fig. 2.

Extracting collected motions and correlated motions of pTsr in complex with (R)-DHMA and (S)-DHMA using principal component analysis and dynamic cross correlation

Principal component analysis (PCA) was used to investigate collected motions within the multiple multi-ns MD simulations of (*R*)- and (*S*)-DHMA in complex with pTsr. PCA has been implemented in similarly modeled systems of the homologous pTar in complex with agonist compounds to extract piston-like motions (14), as well as applied to other proteins involved in chemotaxis (31), ATP generation (32), cancer (33), and HIV (34). Throughout the simulations of both (*R*)- and (*S*)-DHMA in complex with pTsr, we observed an oscillatory piston-like motion in α-helix 4 of pTsr and extracted the principal motions due to (*R*)- and (*S*)-DHMA binding. We performed PCA based on pTsr Cα atoms using Wordom (22). In preparation for PCA, the five simulation trajectories of (*R*)- and (*S*)-DHMA binding to pTsr were independently combined and aligned using Cα atoms. We calculated the covariance matrix of the deviations in Cα atom positions with respect to the average structure using the combined and aligned mul-

tiple multi-ns MD simulations. The covariance matrix was diagonalized to obtain an orthogonal set of eigenvectors. We subsequently analyzed the eigenvectors with the largest eigenvalues within the multiple multi-ns MD simulations.

We also performed dynamic cross correlation (DCC) analysis to examine the correlated motions between the residues within the ligand-binding site and the residues in α-helix 4 associated with the piston-like motions of pTsr. We created DCC maps of the dynamic cross-correlated displacements of Cα atoms throughout the multiple multi-ns MD simulations for both (*R*)- and (*S*)-DHMA, as in (34,35). The analysis does not provide information about the magnitude of the motions, which can be small local oscillations or large-scale collective motions. Complete correlation corresponds to motions with the same phase and period (36,37).

Experimental methods

Separation of (R)- and (S)-DHMA

Separation of (*R*)- and (*S*)-DHMA was achieved using high-performance liquid chromatography (HPLC) with a chiral stationary-phase column. We screened commercially available racemic DHMA (American Custom Chemicals, San Diego, CA) in several analytical columns with different chiral stationary phases and found that a CHIRALPAK ID-3 (150 × 4.6 mm I.D., 3 μm) column provided good resolution using methanol/water (10:90) with 0.1% formic acid as the mobile phase. On the analytical HPLC column, the enantiomers of DHMA had retention times of 4.0 and 5.9 min, and we assigned the (*R*)- and (*S*)-configuration, respectively, as described in Results. To isolate milligram quantities of each enantiomer, the separation was carried out on a semipreparative CHIRALPAK ID (250 × 20 mm I.D., 5 μm) column using methanol/water (20:80) with 0.1% formic acid as the mobile phase. We took advantage of the more-rapid reaction kinetics to prepare acetylated (*S*)-DHMA in high yield and to assign the absolute configuration to each enantiomer. Acetylated (*S*)-DHMA and nonacetylated (*R*)-DHMA were separated by reversed-phase semipreparative HPLC using a C18 column after workup of the reaction; DHMA was not stable to silica gel chromatography (see Supporting Material for details).

Tethered-cell assay

The tethered-cell assay was carried out as described by Berg et al. (38), with slight modifications. A $\Delta cheRB$ derivative of *E. coli* strain RP437 (39), called PL138 (this work), was employed in the assays. The strain carried a genomic variant of the native *fliC* allele that enabled tethering of the cells to glass surfaces (38). Cells were grown in tryptone broth at 33°C, harvested at an OD$_{600}$ of 0.5, and washed and resuspended in motility buffer (10 mM potassium phosphate buffer, 67 mM NaCl, 0.1 mM EDTA, 10 mM sodium lactate, 0.001 mM *L*-methionine, pH 7.0). The flagellar filaments were sheared to stubs, and the cells were tethered to a glass coverslip, which was then placed onto the perfusion chamber (40). Cell rotation was imaged and recorded at 60 fps using an upright light microscope (Optihot-2; Nikon, Tokyo, Japan) with a 20× phase objective and a digital camera (UI-3240LE-M-GL; IDS Imaging Development Systems, Obersulm, Germany). The videos were analyzed with custom-written MATLAB codes to determine the rotational speed of the cells as a function of time, with negative and positive values indicating clockwise (CW) and counterclockwise (CCW) directions of rotation, respectively (41). The mean rotational biases of individual cells over time were determined from Gaussian fits to speed distributions.

Microfluidic chemotaxis assay

The motility migration coefficient (MMC) was determined as described by Pasupuleti et al. (7). Briefly, a strain of wild-type *E. coli* RP437 (39) expressing green fluorescent protein (GFP) from plasmid pCM18 (42) was grown at 30°C in tryptone broth containing 100 μg/mL erythromycin, harvested at an OD$_{600}$ of 0.5, and washed and resuspended in motility buffer.

Dead, RFP-expressing TG1 cells were mixed with the RP437 cells suspended in motility buffer, and the assay was performed within 20 min of preparation. The cell suspension was introduced into the microfluidic device in the middle of the flow channel, and DHMA solutions of equal concentration prepared in motility buffer were introduced on both sides of the introduced cells. The flow rate was maintained at 2.1 μL/min, and images of the cells 1.7 cm down the 2-cm channel were recorded every 2.5 s using a confocal fluorescence microscope (SP8; Leica, Wetzlar, Germany). 400 images were collected for each assay, and the location of the motile, GFP-expressing cells, determined by image analysis, was used to calculate the MMC. The dead, RFP-expressing TG1 cells remained in a thin stream in the exact middle of the channel, demonstrating that the flow was laminar.

RESULTS

Computational results

Investigating (R)-DHMA and (S)-DHMA in complex with pTsr using multiple MD simulations

The initial structures of both (*R*)-DHMA and (*S*)-DHMA were conserved in all of their respective MD simulations (five independent 100-ns simulations per enantiomer). The low average RMSD of both enantiomers with respect to their initial docked position in each of the five simulations (ranging from 1.2 to 1.7 Å for (*R*)-DHMA and 1.3 to 1.7 Å for (*S*)-DHMA, Fig. S2, *A* and *B*) demonstrated that the two ligands do not deviate significantly from their docked positions throughout the individual simulations. The low average RMSD of both enantiomers with respect to their average structure within each of the individual simulations (ranging from 0.9 to 1.1 Å for (*R*)-DHMA and 0.7 to 1.2 Å for (*S*)-DHMA, Fig. S2, *C* and *D*) indicates that the ligands are stable throughout each of the individual simulations. The low average RMSD of both enantiomers with respect to their average structure within their combined five 100-ns MD simulations signifies that the orientation of the two ligands within their respective set of simulations (0.9 ± 0.4 Å for (*R*)-DHMA and 1.0 ± 0.5 Å for (*S*)-DHMA, Fig. S2, *E* and *F*) is reproduced across the multiple multi-ns simulations. However, the relatively high average RMSD of (*R*)-DHMA with respect to the average structure of (*S*)-DHMA and the high average RMSD of (*S*)-DHMA with respect to the average structure of (*R*)-DHMA (excluding the chiral hydroxyl group; 3.0 ± 0.2 and 3.0 ± 0.2 Å, respectively) demonstrates that the orientation of the two enantiomers within the binding site differs. Thus, specific interactions of key pTsr residues with (*R*)- and (*S*)-DHMA are expected to also differ.

We used a combination of hydrogen bond, ligand-protein contact, and per-residue interaction free energy analyses to uncover the key interactions between pTsr residues and the two ligands and their energetic contribution per residue. These interactions persist throughout the duration of the five replicate simulations and are consistent across all five replicates; they are presented in Fig. 3. Within their simulations, both (*R*)-DHMA and (*S*)-DHMA form strong interactions with pTsr residues in the serine-binding site (Figs. 3
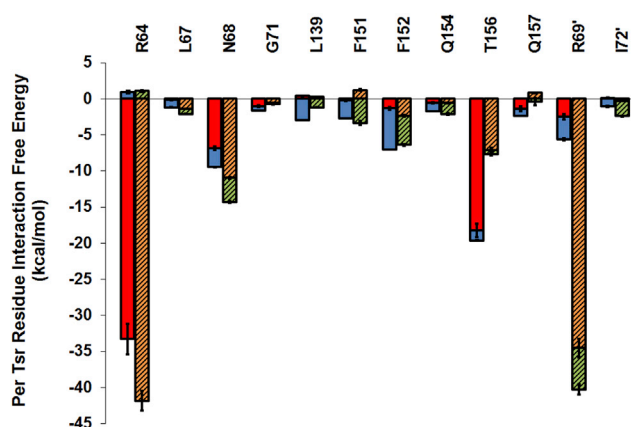

FIGURE 3 Per-pTsr residue interaction free energies for interactions with free energy values less than −1 kcal/mol. The first set of bars (*solid red* and *blue*) per pTsr residue corresponds to interaction free energies between the Tsr residue and (*R*)-DHMA. The second set of bars (*striped orange* and *green*) per pTsr residue corresponds to interaction free energies between the pTsr residue and (*S*)-DHMA. For each pTsr residue, the interaction free energy is decomposed into polar (*gray red* and *orange*) and nonpolar (*blue* and *green bars*) components. Error bars correspond to the standard deviation of the per-pTsr residue interaction free energy averaged over the number of simulation snapshots and the five replicate MD simulations. To see this figure in color, go online.

and 4). The negatively charged carboxyl group of both enantiomers forms salt bridges with the positively charged guanidino group of Arg64. Additionally, the carboxyl group of both enantiomers forms a hydrogen bond with the side-chain hydroxyl group of Thr156 and with Asn68. Hydrogen bonds are also formed by the three-hydroxyl group of the aromatic ring of both enantiomers with the backbone amide group of Phe151. In addition to their similar polar interactions, the aromatic rings of (*R*)- and (*S*)-DHMA form π-π interactions with the aromatic rings of Phe151 and Phe152. Both enantiomers are also involved in van der Waals interactions with Leu67, Leu139, and Ile72′.

Despite the structural similarity of (*R*)-DHMA and (*S*)-DHMA, they adopt different orientations within the pTsr binding pocket (Fig. 4), as indicated by the relatively large RMSD values of (*R*)-DHMA compared with (*S*)-DHMA, and vice versa. Compared with (*R*)-DHMA, (*S*)-DHMA forms a significantly stronger interaction with Arg69′ (Fig. 3). (*R*)-DHMA forms only a hydrogen bond with Arg69′, whereas (*S*)-DHMA forms both salt-bridge and cation-π interactions. Additionally, the hydrogen bond between (*R*)-DHMA and Arg69′ is mediated by water molecules in 19.6% of the simulation snapshots. On the other hand, the interaction free energy between Thr156 and (*S*)-DHMA is only half that of (*R*)-DHMA (Fig. 3). Whereas (*R*)-DHMA forms hydrogen bonds with both side-chain and backbone atoms of Thr156, (*S*)-DHMA forms only one hydrogen bond with the side-chain hydroxyl (Fig. 4). (*R*)-DHMA forms a hydrogen bond with the backbone amide group of Thr156 in 68.7% of the simulation snapshots, whereas (*S*)-DHMA forms a hydrogen bond with
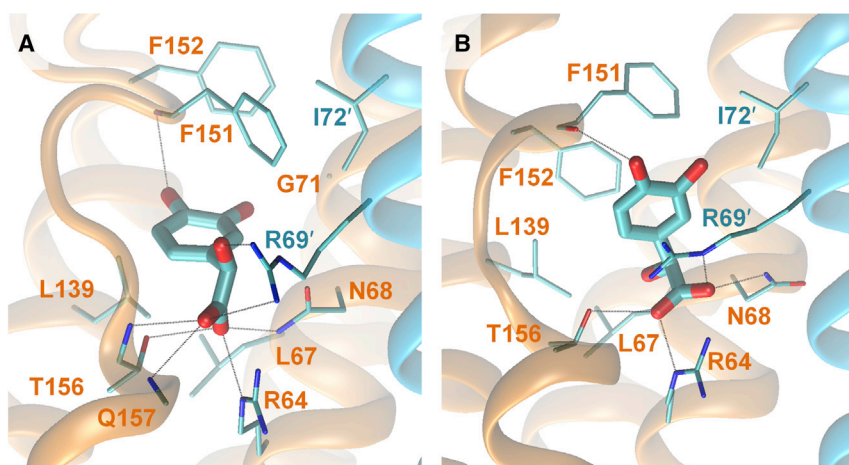
FIGURE 4 Molecular graphic images of (*A*) (*R*)-DHMA and (*B*) (*S*)-DHMA in complex with *E. coli* pTsr. The majority binding site of pTsr is shown in an orange transparent cartoon representation; the minority binding site is shown in a cyan transparent cartoon representation. (*R*)-DHMA and (*S*)-DHMA are shown in cyan, with oxygen atoms in red. Key pTsr residues are shown in stick representations and are labeled in orange (majority side) or cyan (minority side). Black dotted lines indicate hydrogen bonds. To see this figure in color, go online.

the backbone amide group of Thr156 in only 0.1% of the simulation snapshots. Additionally, although the carbonyl group of (*R*)-DHMA forms water-mediated interactions with either the side-chain or backbone amide group of Thr156 in only 2.4% of the simulation snapshots, the carbonyl group of (*S*)-DHMA forms water-mediated interactions with the side-chain and backbone amide groups of Thr156 in 34.7 and 18.2% of the simulation snapshots, respectively. Water molecules greatly weaken the interaction between two polar molecules (43). The interaction free energy calculations show that the interaction between Arg69′ and (*R*)-DHMA is weaker than the interaction between Arg69′ and (*S*)-DHMA and that the interaction between Thr156 and (*S*)-DHMA is weaker than the interaction between Thr156 and (*R*)-DHMA. These differences can partly be attributed to the presence of water mediating these interactions. These differences between the binding of (*R*)-DHMA and (*S*)-DHMA to pTsr likely lead to differences in the allosteric effects their binding elicits.

Investigating piston-like motions in pTsr caused by binding of (R)-DHMA and (S)-DHMA

The crystal structures of the unbound and serine-bound *E. coli* pTsr suggest that conformational changes in α-helix 4 of Tsr are important for signaling (13). We tracked the projected lengths of α-helix 4 throughout the simulations to understand the conformational dynamics of pTsr bound to (*R*)- and (*S*)-DHMA as well as to predict and compare the Tsr strength of the signal induced by the two ligands. The projected lengths with respect to time for each of the five replicate multi-ns simulations are plotted in Fig. 5. As controls, we also tracked projected lengths for five 100-ns MD simulations of serine in complex with pTsr and two 100-ns MD simulations of apo pTsr. The starting structure of the former corresponded to the experimentally resolved structure of the pTsr-serine complex (13), except that the second bound serine ligand with disordered electron density (13) was removed. The starting structure of the latter corresponded to the experimentally

resolved structure of the pTsr-serine complex (13) with both bound serine ligands removed. For the simulations of serine in complex with pTsr, the average projected length for the downward motion of α-helix 4 was 0.92 ± 0.08 Å (Fig. S3 *A*), an average value that deviates from the crystal structure by only 0.08 Å. For the simulations of the apo pTsr, the projected length approached zero as the simulations progressed, and after 50 ns, the average projected length was only 0.11 ± 0.12 Å (Fig. S3 *B*). Thus, the simulated apo pTsr returned to the conformation of the apo pTsr crystal structure (13). These results suggest that the modeled systems and the simulation duration of (*R*)- and (*S*)-DHMA in complex with pTsr were sufficiently accurate to investigate signaling induced by the two ligands. They also indicate that the projected lengths can be used as a metric to predict the strength of the signal induced by the two ligands. Additional details on the MD simulations and subsequent analysis of serine-bound and apo pTsr are provided in Supporting Material.

Our analysis shows that (*R*)-DHMA induces a larger motion of the α-helix 4 toward the membrane than (*S*)-DHMA. The average projected length for (*R*)-DHMA is 1.08 ± 0.15 Å, whereas that for (*S*)-DHMA is 0.69 ± 0.07 Å. By evaluating the projected lengths as a function of time, we observed that α-helix 4 oscillates throughout the MD simulations (Fig. 5). Although the simulations of both enantiomers in complex with pTsr show piston-like motions in the helix, the peak values with (*R*)-DHMA are higher than with (*S*)-DHMA; the maximal projected length after 50 ns with (*R*)-DHMA is 2.12 Å, whereas the maximal projected length with (*S*)-DHMA is 1.26 Å. The presence of larger piston-like motions with (*R*)-DHMA indicates that (*R*)-DHMA induces a stronger allosteric signal than (*S*)-DHMA.

Extracting collected motions of pTsr in complex with (R)-DHMA and (S)-DHMA using PCA

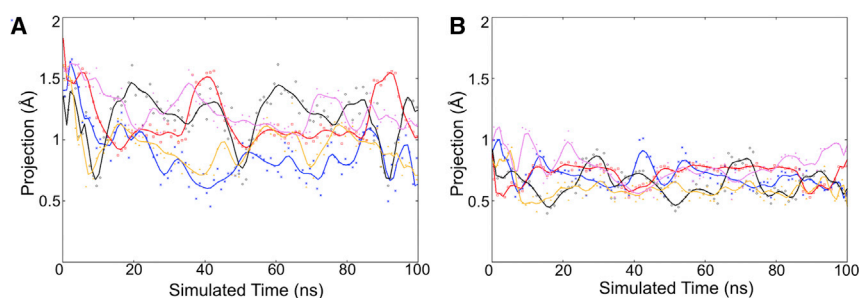We performed PCA on the Cα atomic positions throughout the combined five replicate trajectories for both (*R*)- and

FIGURE 5 Vector projections showing the normalized magnitude of piston-like motions (in Å) within α-helix 4 of pTsr bound to (A) (R)-DHMA and (B) (S)-DHMA with respect to the simulated time (in nanoseconds). The projection values plotted correspond to projected lengths, p_i, calculated using Eq. 2 and extracted every 1 ns. Solid lines correspond to Bezier curves fitted to projected lengths extracted every 0.1 ns. Blue, red, black, yellow, and pink data points and lines correspond to data extracted from the first, second, third, fourth, and fifth simulations, respectively, for each of the complexes. The differences in initial points are attributed to the initial structure corresponding to the binding mode identified by our docking-refinement protocol as well as the use of a short equilibration stage before the 100-ns MD simulations. To see this figure in color, go online.

(S)-DHMA to extract the principal motions occurring within the multiple multi-ns simulations. According to PCA, the first eigenvector of the simulations with (R)- and (S)-DHMA corresponds to a piston-like motion of α-helix 4 of pTsr (Fig. 6). The first eigenvector accounts for 35.35 and 24.76%, respectively, of the motions observed in the simulations of the (R)-DHMA-pTsr and (S)-DHMA-pTsr complexes. In line with our aforementioned analysis on the projected motions of the helix, the amplitude of the motion within the first eigenvector for residues 158–172 is larger with (R)-DHMA than with (S)-DHMA. These results complement the calculated projected lengths, providing further evidence that (R)-DHMA should be a stronger chemoattractant than (S)-DHMA.

Extracting correlated motions of pTsr in complex with (R)-DHMA and (S)-DHMA using DCC

To understand how, and to what extent, different interactions within the binding pocket correlate with the observed differences in the motion of α-helix 4, we performed DCC analysis. The DCC maps are shown in Fig. 7. The maps are quite similar for (R)- and (S)-DHMA. However, we observed a different correlation of motion for residues within the binding site (148–156) and residues in α-helix 4 (156–185). These are marked by the green box in Fig. 7. For both ligands, apart from the expected correlated motions among nearby residues in the pTsr sequence (the diagonal in Fig. 7), the motions of residues within the same α-helix and residues in proximal α-helices are correlated.

The correlated motions of pTsr binding to (R)- and (S)-DHMA differ in the motions of the binding site residues and α-helix 4 residues (marked by the green box in Fig. 7). With (R)-DHMA, the motions of residues in α-helix 4 are highly correlated with the movement of residues in the binding site. In contrast, with (S)-DHMA, the motions of α-helix 4 residues are weakly correlated or anticorrelated with the movement of residues in the binding site. Specifically, with (R)-DHMA, the contraction of residues 148–156 into the binding site correlates with the downward motion of α-helix 4. Thus, differences in the piston-like motions observed in the simulations of (R)- and (S)-DHMA binding

to pTsr are due to differences in their interactions with residues in the ligand-binding pocket.

To understand which interactions are most important for the contraction of the ligand-binding site residues, we extracted the simulation snapshots of pTsr binding to (R)-DHMA in which α-helix 4 was or was not pushed down. We observed that when the helix is pushed downward, (R)-DHMA forms a hydrogen bond with both the backbone amide group and the side-chain hydroxyl group of Thr156. When the helix is not pushed down, (R)-DHMA forms a hydrogen bond only with the side-chain hydroxyl group of Thr156. When (R)-DHMA forms hydrogen bonds with both the backbone and side chain of Thr156, the residues of the binding site contract into the binding site, and this contraction pushes α-helix 4 downward (Fig. 6). This event is not observed in the simulations of pTsr binding to (S)-DHMA. (R)-DHMA forms a hydrogen bond to the amide group of Thr156 in 68.7% of the simulation snapshots, whereas (S)-DHMA forms a hydrogen bond to the amide group of Thr156 in only 0.1% of the simulation snapshots. Thus, all of our computational analyses agree in suggesting that (R)-DHMA should be a stronger chemoattractant than (S)-DHMA. Thus, we conclude that (R)-DHMA was the key contributor to the previously reported chemotaxis to racemic DHMA (7,10). The final MD simulation snapshots are provided in PDB format as part of the Supporting Material.

Experimental results

Resolution and determination of the absolute configuration of (R)-DHMA and (S)-DHMA

The resolution of (R)- and (S)-DHMA was achieved using HPLC with a chiral stationary-phase column. We screened commercially available racemic DHMA in several analytical columns with different chiral stationary phases and found that a CHIRALPAK ID-3 (150 × 4.6 mm I.D., 3 μm) column provided good resolution when methanol/water (10:90) containing 0.1% formic acid was used as the mobile phase. On the analytical HPLC column, the enantiomers of DHMA had retention times of 4.0 and 5.9 min, and we
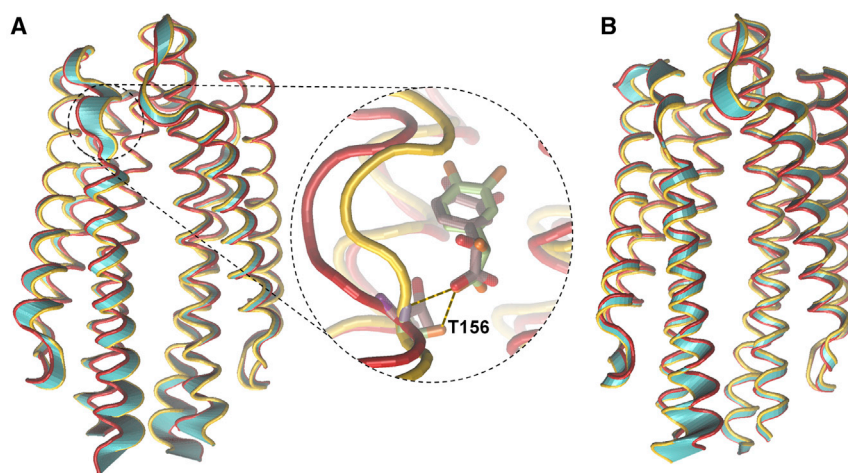
assigned them the (*R*) and (*S*) configurations, respectively. To isolate milligram quantities of each enantiomer, the separation was carried out by HPLC using a preparative CHIRALPAK ID (250 × 20 mm I.D., 5 μm) column with methanol/water (20:80) containing 0.1% formic acid as the mobile phase (see Supporting Material for details).

To assign the configuration of each isolated enantiomer, we used a lipase-catalyzed kinetic resolution technique described for secondary alcohols (44). We selected this method because of the structural similarity between DHMA and secondary alcohols whose configuration has been accurately assigned using this approach (45). Additionally, a significant difference in the size of the substituents attached to the secondary alcohol (phenyl versus carboxylic acid) greatly improves the reliability of the assignment. Thus, reaction of racemic DHMA with vinyl acetate and commercially available Amano Lipase PS for 24 h at room temperature provided acetate **3** in 41% isolated yield and enantiomerically enriched (*R*)-DHMA **2** in 45% yield (Fig. 8). Analysis of unreacted DHMA **2** by HPLC using the CHIRALPAK ID column indicated that it was highly enriched in the faster-eluting enantiomer (94:6 ratio, 88% enantiomeric excess (ee), RT = 6.9 min for the pre-

dominant isomer on the preparative column). Because the empirical rule of the lipase kinetic resolution method (44) predicts that the (*S*)-enantiomer of DHMA should react faster to form acetate **3**, the unreacted enantiomer **2** was assigned the (*R*) configuration. This assignment agrees with the assignment reported for the kinetic resolution of structurally similar mandelic acid (45).

Tethered-cell assay

To determine the relative effectiveness of (*R*)- and (*S*)-DHMA as attractants, we employed the tethered-cell assay. The limited availability of the separated enantiomers required that we choose one optimum concentration, with 2 mM giving the clearest responses. The strain used in these experiments, PL138, was a derivative of strain RP437 (39) deleted for the *cheRB* genes (*ΔcheRB*) and containing a *fliC* allele that produces "sticky" flagella that facilitate spontaneous tethering to a glass surface. Tethered cells were first subjected to continuous flow of motility buffer in the microfluidic device, and the mean CW bias was analyzed over the initial 2 min. Cells used in the analysis were chosen to have a prestimulus CW bias of 0.8–0.9.
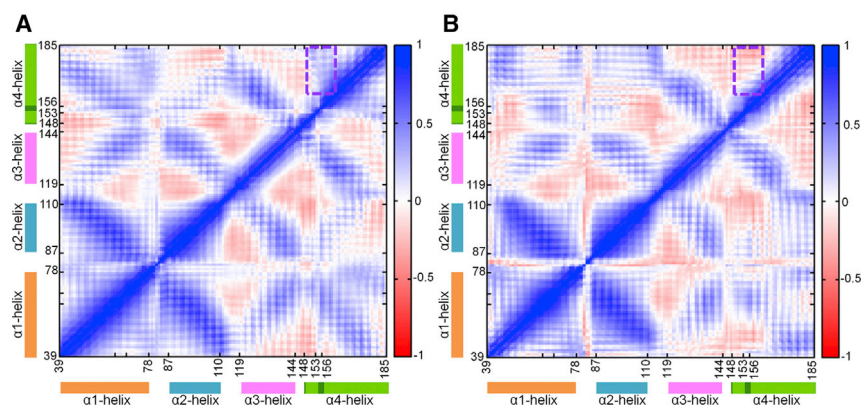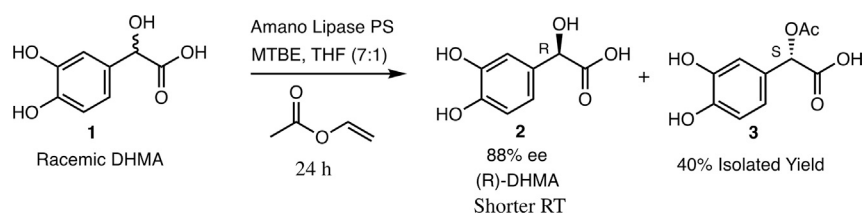
FIGURE 8 Kinetic resolution of racemic DHMA. Reaction of racemic DHMA with vinyl acetate and commercially available Amano Lipase PS for 24 h at room temperature provided acetate **3** in 41% isolated yield and enantiomerically enriched (*R*)-DHMA **2** in 45% yield.

Cells were then exposed to a step stimulus by flowing 2 mM (*R*)- or (*S*)-DHMA in motility buffer into the chamber. The CW biases decreased immediately after introduction of either enantiomer and remained stable or continued to decrease slowly over the next 100 s. The response to (*R*)-DHMA was clearly stronger, with a stabilized CW bias of ∼0.4 (Fig. 9). The response to (*S*)-DHMA was also rapid, but the stabilized CW bias was ∼0.6 (Fig. 9), indicating a decreased attractant response compared with (*R*)-DHMA. The stronger response to (*R*)-DHMA is consistent with the predictions of the simulations.

The MMC assay

The responses to (*R*)- and (*S*)-DHMA were also measured in the MMC assay, which records the increased spreading of cells as a consequence of increased smooth swimming. Again, because of a limited supply of the two separated enantiomers, only data for the two concentrations that showed the clearest results are shown. In this assay, motile cells are introduced into the middle of the flow channel, and the distribution across the channel of the GFP-expressing RP437 cells 1.7 cm down the channel was determined by fluorescence microscopy. When the channel was perfused with the same motility buffer as that in which the cells were suspended, the MMC coefficient due to random motility was ∼0.08 (Fig. 10). When the channel was perfused with motility buffer containing (*R*)- or (*S*)-
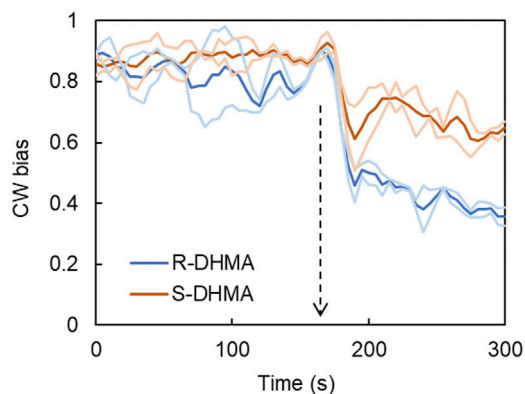
DHMA dissolved in motility buffer at 50 μM, the MMC value for (*R*)-DHMA doubled to ∼0.16, whereas the MMC value for *S*-DHMA remained at 0.08. When the experiment was repeated with 500 μM DHMA, the MMC value for (*R*)-DHMA rose to ∼0.27, and a smaller, but still significant, response of ∼0.16 was seen with (*S*)-DHMA. Thus, in agreement with the results from the tethered-cell assay, both (*R*)- and (*S*)-DHMA evoked a smooth-swimming (CCW-biased) response, but the response to (*R*)-DHMA appeared at a lower concentration and was of a greater magnitude.

DISCUSSION

The study of protein-ligand interactions is key for prediction of protein function and drug design. With advances in computational power, molecular docking and MD simulation have become fundamental tools for investigating protein-ligand interactions at an atomic level (35,46–50). A number of docking methods have been released, which among others, include (51–66). Docking programs can predict docked poses with RMSDs averaging between 1.5 and 2 Å relative to the experimentally resolved structure (67). However, flexible receptor docking, particularly with flexibility in the receptor backbone, remains a major challenge for current docking algorithms (68). According to a recent review by Chaput and Mouawad on four popular docking programs (69), there is still a weakness in the ability of the scoring functions to detect the correct poses. Despite the associated additional computational cost, MD simulations combined with physics-based calculations of free energy can prove beneficial for detecting the lowest binding free energy mode of a protein-protein, peptide-protein, or compound-protein complex (15–20,28,70–76). Furthermore, MD simulations are a useful tool for investigating allosteric changes in a receptor induced by ligand binding (14,31–34,77–84).

The catechol-containing compound that interacts with the *E. coli* Tsr chemoreceptor is DHMA (7). Initial studies used a racemic mixture of the (*R*) and (*S*) enantiomers, leaving open the question of which chiral form is active. Separation of the two enantiomers in amounts suitable for studies of chemotaxis is time-consuming and requires specialized chiral columns. To decide whether it was worthwhile to go to this effort, we first studied the binding of the two enantiomers to pTsr using a nearly exhaustive, highly accurate

FIGURE 9 The tethered-cell response of an *E. coli* Δ*cheRB* strain to 2 mM (*R*)- and (*S*)-DHMA. The CW bias was calculated from the CW/CCW ratio of flagellar rotation. The response was averaged from two separate experiments, each including at least 12 motors. The faint lines represent the standard deviation. The arrow indicates the beginning of DHMA perfusion. To see this figure in color, go online.
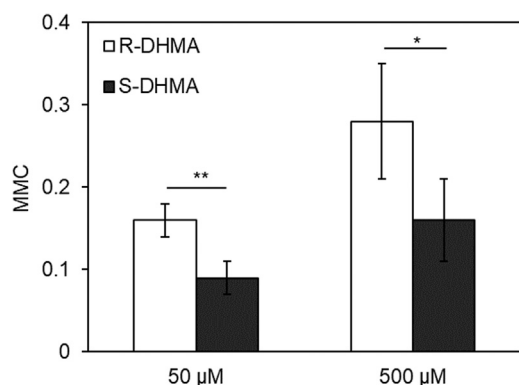
FIGURE 10 The chemotaxis response of wild-type *E. coli* to 50 and 500 μM of (*R*)-DHMA and (*S*)-DHMA. The response was averaged from three separate experiments. The error bars indicate the standard deviation. Statistical significance is indicated for the comparison of responses to (*R*)-DHMA and (*S*)-DHMA using the Student's *t*-test at a significance level of $p < 0.01$ (**) for 50 μM and of $p < 0.04$ (*) for 500 μM DHMA.

computational docking procedure combined with MD simulations and physics-based free energy calculations. This combination proved especially beneficial because short MD simulations introduced flexibility into pTsr and allowed refinement of the initial structures of the candidate binding modes before selecting the most energetically favorable ones for further investigation. The independent use of harmonic and spherical potentials constraining (*R*)- and (*S*)-DHMA within the binding pocket during the docking procedure enabled us to explore binding modes both away from (quartic) and in proximity to (harmonic) their initial position. Notably, the most energetically favorable binding mode of (*R*)-DHMA was derived using a quartic spherical potential (15), whereas the most energetically favorable binding mode of (*S*)-DHMA was derived using a harmonic spherical potential. A similar approach was used previously to determine how subtle differences between similar flavonoids binding to the aryl hydrocarbon receptor could explain their serving as agonists or antagonists (17,20). Multiple multi-ns MD simulations, using all-atom force fields (21) coupled with PCA and DCC analysis, allowed us to study in detail the complex formation and allosteric changes in pTsr caused by ligand binding.

In five replicate 100-ns simulations of serine in complex with pTsr, the average projected length deviated from the crystal structure by only 0.08 Å. Two supplementary 100-ns simulations of apo pTsr (with both resolved serine ligands removed), using the crystal structure of pTsr bound by serine (13) as the initial structure, show that the projected length approached zero as the simulations progressed. Thus, the simulated apo pTsr returned to the conformation of the apo pTsr crystal structure (13). These results demonstrate that our simulation system captures how differences in the binding site correlate with piston-like motions of α-helix 4. Thus, despite the fact that the entire Tsr protein was not used in the simulations, the modeled systems of (*R*)- and

(*S*)-DHMA in complex with pTsr were sufficiently large to understand signaling induced by the two ligands.

The MD simulations and structural analyses strongly suggested that binding of (*R*)-DHMA causes a larger contraction of the binding pocket than binding of (*S*)-DHMA. This contraction is correlated with a larger downward piston-like motion of α-helix 4 than was seen with (*S*)-DHMA, leading to our prediction that (*R*)-DHMA is a stronger attractant than (*S*)-DHMA. (*R*)-DHMA forms weaker interactions to Arg69′ than (*S*)-DHMA. DHMA forms hydrogen bonds with both its chiral OH group and the negatively charged carboxyl group of pTsr. (*S*)-DHMA forms a single hydrogen bond to Arg69′ with its negatively charged carboxyl group and a cation-π interaction to Arg69′ with its aromatic ring. Because of the different orientations of (*R*)- and (*S*)-DHMA caused by their different chirality, (*R*)-DHMA forms hydrogen bonds to both the side chain and backbone of Thr156, whereas (*S*)-DHMA forms a hydrogen bond only with the side chain of Thr156. Hydrogen bonds between (*R*)-DHMA and Arg69′ as well as (*S*)-DHMA and Thr156 are occasionally mediated by water molecules, weakening their interaction.

We also observed correlated motions of residues within the binding site with residues in α-helix 4. Interactions of (*R*)-DHMA with both the side-chain and backbone atoms of Thr156 induce conformational changes within the binding pocket that displace α-helix 4 downward. The counterpart of Thr156 in the Tar chemoreceptor, Thr154, has been implicated in the piston-like movement of α-helix 4 in response to the binding of the attractant *L*-aspartate (14), and Thr156 of Tsr is essential for attractant responses to DHMA (7). Our computational prediction that (*R*)-DHMA should be a stronger chemoattractant than (*S*)-DHMA encouraged us to undertake the separation of the two enantiomers and to test their efficacy as chemoattractants.

Separation of (*R*)- and (*S*)-DHMA was achieved using HPLC with a chiral stationary-phase column (semipreparative CHIRALPAK ID). Analysis of the two isolated enantiomers demonstrated that the (R)-DHMA was >98% ee and the (S)-DHMA was in 94% ee. In this way, sufficient amounts of the two highly enriched enantiomers were generated for use in chemotaxis assays.

In the tethered-cell assay, addition of 2 mM (*R*)-DHMA to Δ*cheRB* cells caused a decrease in the CW bias from 80 to 40% that persisted for at least 100 s. Addition of 2 mM (*S*)-DHMA decreased the CW bias from 80 to 60%, again for a period of at least 100 s. Thus, although both enantiomers at an equivalent concentration increased CCW rotation, (*R*)-DHMA had a larger effect. In the MMC assay, exposure of wild-type (RP437) cells to (*R*)-DHMA produced an increase in smooth swimming at concentrations of 50 and 500 μM, with a larger increase seen with 500 μM. In comparison, (*S*)-DHMA did not increase smooth swimming at 50 μM, and at 500 μM, it was only

as effective as (*R*)-DHMA at 50 μM. Thus, two different assays supported the prediction from the simulations that both enantiomers of DHMA might serve as chemoattractants but that (*R*)-DHMA would be more potent than (*S*)-DHMA.

DHMA is generated in the gut by the resident microbiota (10), presumably as a racemic mixture of the two enantiomers, although the chiral form(s) in the gut have not been determined experimentally. The racemic mixture in vitro loses its potency as an attractant at higher concentrations (7). This observation is consistent with the report that DHMA at high concentrations serves as a repellent (11). In a heterodimeric Tsr designed to bind DHMA at only one of its two ligand-binding sites, DHMA served as an attractant at all concentrations tested (7). In future studies, it will be interesting to determine how binding at the second site cancels out the attractant response and whether one enantiomer or both of them are responsible for this effect. It also remains to be determined how attractant and repellent responses to DHMA may serve to control the migration of *E. coli*, and potentially other motile gut bacteria, in the intestinal tract.

Our study demonstrates how refined computational docking and simulation studies can be combined with experiments to investigate biological phenomena in which subtle differences between ligands may lead to diverse binding-mediated outcomes. The computational results provided the impetus to carry out the separation of the two chiral forms of DHMA. After the two enantiomers were separated, they could be used to assay the function of each enantiomer as a chemoattractant. In this instance, the predictions from computational docking and simulations were supported by the experiments. Our study could serve as a model for additional collaborative efforts to address questions involving the different activities of closely related chemical compounds as signaling molecules or enzyme substrates.

SUPPORTING MATERIAL

Supporting Material can be found online at https://doi.org/10.1016/j.bpj.2019.11.3382.

AUTHOR CONTRIBUTIONS

A.J., M.D.M., and P.T. conceived the project. A.J., M.D.M., and P.T. supervised the project. All authors contributed to the analysis and writing of the manuscript.

ACKNOWLEDGMENTS

SUPPORTING CITATIONS

References (85–94) appear in the Supporting Material.

REFERENCES

1. Surette, M. G., M. B. Miller, and B. L. Bassler. 1999. Quorum sensing in *Escherichia coli, Salmonella typhimurium*, and *Vibrio harveyi*: a new family of genes responsible for autoinducer production. *Proc. Natl. Acad. Sci. USA.* 96:1639–1644.

2. Hegde, M., D. L. Englert, …, A. Jayaraman. 2011. Chemotaxis to the quorum-sensing signal AI-2 requires the Tsr chemoreceptor and the periplasmic LsrB AI-2-binding protein. *J. Bacteriol.* 193:768–773.

3. Miller, S. T., K. B. Xavier, …, F. M. Hughson. 2004. *Salmonella typhimurium* recognizes a chemically distinct form of the bacterial quorum-sensing signal AI-2. *Mol. Cell.* 15:677–687.

4. Springer, M. S., M. F. Goy, and J. Adler. 1977. Sensory transduction in *Escherichia coli*: two complementary pathways of information processing that involve methylated proteins. *Proc. Natl. Acad. Sci. USA.* 74:3312–3316.

5. Laganenka, L., R. Colin, and V. Sourjik. 2016. Chemotaxis towards autoinducer 2 mediates autoaggregation in *Escherichia coli. Nat. Commun.* 7:12984.

6. Jani, S., A. L. Seely, …, M. D. Manson. 2017. Chemotaxis to self-generated AI-2 promotes biofilm formation in *Escherichia coli. Microbiology.* 163:1778–1790.

7. Pasupuleti, S., N. Sule, …, M. D. Manson. 2014. Chemotaxis of *Escherichia coli* to norepinephrine (NE) requires conversion of NE to 3,4-dihydroxymandelic acid. *J. Bacteriol.* 196:3992–4000.

8. Rankin, L. D., D. M. Bodenmiller, …, S. Spiro. 2008. *Escherichia coli* NsrR regulates a pathway for the oxidation of 3-nitrotyramine to 4-hydroxy-3-nitrophenylacetate. *J. Bacteriol.* 190:6170–6177.

9. Eisenhofer, G., I. J. Kopin, and D. S. Goldstein. 2004. Catecholamine metabolism: a contemporary view with implications for physiology and medicine. *Pharmacol. Rev.* 56:331–349.

10. Sule, N., S. Pasupuleti, …, A. Jayaraman. 2017. The norepinephrine metabolite 3,4-dihydroxymandelic acid is produced by the commensal microbiota and promotes chemotaxis and virulence gene expression in enterohemorrhagic *Escherichia coli. Infect. Immun.* 85:e00431-17.

11. Lopes, J. G., and V. Sourjik. 2018. Chemotaxis of *Escherichia coli* to major hormones and polyamines present in human gut. *ISME J.* 12:2736–2747.

12. Meirieu, O., M. Pairet, …, M. Ruckebusch. 1986. Local release of monoamines in the gastrointestinal tract: an in vivo study in rabbits. *Life Sci.* 38:827–834.

13. Tajima, H., K. Imada, …, I. Kawagishi. 2011. Ligand specificity determined by differentially arranged common ligand-binding residues in bacterial amino acid chemoreceptors Tsr and Tar. *J. Biol. Chem.* 286:42200–42210.

14. Yu, D., X. Ma, …, L. Lai. 2015. Both piston-like and rotational motions are present in bacterial chemoreceptor signaling. *Sci. Rep.* 5:8640.

15. Orr, A. A., A. Jayaraman, and P. Tamamis. 2018. Molecular modeling of chemoreceptor:ligand interactions. *Methods. Mol. Biol.* 1729:353–372.

16. Jin, U. H., Y. Cheng, …, S. Safe. 2017. Short chain fatty acids enhance aryl hydro carbon (Ah) responsiveness in mouse colonocytes and Caco-2 human colon cancer cells. *Sci. Rep.* 7:10163.

17. Jin, U. H., H. Park, …, S. Safe. 2018. Structure-dependent modulation of aryl hydrocarbon receptor-mediated activities by flavonoids. *Toxicol. Sci.* 164:205–217.

18. Mohan, R. R., M. Wilson, …, D. Morikis. 2018. Virtual screening of chemical compounds for discovery of complement C3 ligands. *ACS Omega.* 3:6427–6438.

19. Yoon, K., C. C. Chen, …, S. Safe. 2019. Activation of COUP-TFI by a novel diindolylmethane derivative. *Cells.* 8:220.

20. Park, H., U. H. Jin, …, S. Safe. 2019. Isoflavones as Ah receptor agonists in colon-derived cell lines: structure-activity relationships. *Chem. Res. Toxicol.* 32:2353–2364.

21. Brooks, B. R., C. L. Brooks, III, …, M. Karplus. 2009. CHARMM: the biomolecular simulation program. *J. Comput. Chem.* 30:1545–1614.

22. Seeber, M., A. Felline, …, F. Fanelli. 2011. Wordom: a user-friendly program for the analysis of molecular structures, trajectories, and free energy surfaces. *J. Comput. Chem.* 32:1183–1194.

23. Hayes, J. M., and G. Archontis. 2012. MM-GB(PB)SA calculations of protein-ligand binding free energies. *In* Molecular Dynamics - Studies of Synthetic and Biological Macromolecules. L. Wang, ed. InTech, Southern Illinois University Carbondale, pp. 171–190.

24. Tamamis, P., D. Morikis, …, G. Archontis. 2010. Species specificity of the complement inhibitor compstatin investigated by all-atom molecular dynamics simulations. *Proteins.* 78:2655–2667.

25. Tamamis, P., P. Pierou, …, G. Archontis. 2011. Design of a modified mouse protein with ligand binding properties of its human analog by molecular dynamics simulations: the case of C3 inhibition by compstatin. *Proteins.* 79:3166–3179.

26. Tamamis, P., A. López de Victoria, …, G. Archontis. 2012. Molecular dynamics in drug design: new generations of compstatin analogs. *Chem. Biol. Drug Des.* 79:703–718.

27. Kieslich, C. A., P. Tamamis, …, D. Morikis. 2012. Exploring protein-protein and protein-ligand interactions in the immune system using molecular dynamics and continuum electrostatics. *Curr. Phys. Chem.* 2:324–343.

28. Tamamis, P., and C. A. Floudas. 2014. Elucidating a key component of cancer metastasis: CXCL12 (SDF-1α) binding to CXCR4. *J. Chem. Inf. Model.* 54:1174–1188.

29. Samanta, D., P. P. Borbat, …, B. R. Crane. 2015. Bacterial chemoreceptor dynamics correlate with activity state and are coupled over long distances. *Proc. Natl. Acad. Sci. USA.* 112:2455–2460.

30. Kitanovic, S., P. Ames, and J. S. Parkinson. 2011. Mutational analysis of the control cable that mediates transmembrane signaling in the *Escherichia coli* serine chemoreceptor. *J. Bacteriol.* 193:5062–5072.

31. Cassidy, C. K., B. A. Himes, …, P. Zhang. 2015. CryoEM and computer simulations reveal a novel kinase conformational switch in bacterial chemotaxis signaling. *eLife.* 4:e08419.

32. Papachristos, K., S. P. Muench, and E. Paci. 2016. Characterization of the flexibility of the peripheral stalk of prokaryotic rotary A-ATPases by atomistic simulations. *Proteins.* 84:1203–1212.

33. Meng, H., Z. Dai, …, L. Lai. 2018. Molecular mechanism of 15-lipoxygenase allosteric activation and inhibition. *Phys. Chem. Chem. Phys.* 20:14785–14795.

34. López de Victoria, A., P. Tamamis, …, D. Morikis. 2012. Insights into the structure, correlated motions, and electrostatic properties of two HIV-1 gp120 V3 loops. *PLoS One.* 7:e49925.

35. Wang, B., J. Francis, …, M. Feig. 2016. Long-range signaling in MutS and MSH homologs via switching of dynamic communication pathways. *PLoS Comput. Biol.* 12:e1005159.

36. McCammon, A. J., and S. C. Harvey. 1986. Dynamics of Proteins and Nucleic Acids. Cambridge University Press, Cambridge, UK.

37. Brooks, C. L., III, M. Karplus, and B. M. Pettitt. 1988. Proteins: A Theoretical Perspective of Dynamics, Structure and Thermodynamics. John Wiley and Sons, New York.

38. Berg, H. C., and L. Turner. 1993. Torque generated by the flagellar motor of *Escherichia coli. Biophys. J.* 65:2201–2216.

39. Parkinson, J. S., and S. E. Houts. 1982. Isolation and behavior of *Escherichia coli* deletion mutants lacking chemotaxis functions. *J. Bacteriol.* 151:106–113.

40. Berg, H. C., and S. M. Block. 1984. A miniature flow cell designed for rapid exchange of media under high-power microscope objectives. *J. Gen. Microbiol.* 130:2915–2920.

41. Chawla, R., K. M. Ford, and P. P. Lele. 2017. Torque, but not FliL, regulates mechanosensitive flagellar motor-function. *Sci. Rep.* 7:5565.

42. Hansen, M. C., R. J. Palmer, Jr., …, S. Molin. 2001. Assessment of GFP fluorescence in cells of Streptococcus gordonii under conditions of low pH and low oxygen concentration. *Microbiology.* 147:1383–1391.

43. Alberts, B., A. Johnson, and P. Walter. 2008. Molecular Biology of the Cell, Fifth Edition. Garland Science, London, UK.

44. Jing, Q., and R. J. Kazlauskas. 2008. Determination of absolute configuration of secondary alcohols using lipase-catalyzed kinetic resolutions. *Chirality.* 20:724–735.

45. Dabkowska, D., and K. W. Szewczyk. 2009. Influence of temperature on the activity and enantioselectivity of Burkholderia cepacia lipase in the kinetic resolution of mandelic acid enantiomers. *Biochem. Eng. J.* 46:147–153.

46. Naqvi, A. A. T., T. Mohammad, …, M. I. Hassan. 2018. Advancements in docking and molecular dynamics simulations towards ligand-receptor interactions and structure-function relationships. *Curr. Top. Med. Chem.* 18:1755–1768.

47. Burger, V. M., A. Vandervelde, …, C. M. Stultz. 2017. Hidden states within disordered regions of the CcdA antitoxin protein. *J. Am. Chem. Soc.* 139:2693–2701.

48. Burger, V. M., D. J. Arenas, and C. M. Stultz. 2016. A structure-free method for quantifying conformational flexibility in proteins. *Sci. Rep.* 6:29040.

49. Phillips, C. M., P. S. Nerenberg, …, C. M. Stultz. 2009. Physical basis of metal-binding specificity in *Escherichia coli* NikR. *J. Am. Chem. Soc.* 131:10220–10228.

50. Mukherjee, S., and M. Feig. 2009. Conformational change in MSH2-MSH6 upon binding DNA coupled to ATPase activity. *Biophys. J.* 96:L63–L65.

51. Trott, O., and A. J. Olson. 2010. AutoDock Vina: improving the speed and accuracy of docking with a new scoring function, efficient optimization, and multithreading. *J. Comput. Chem.* 31:455–461.

52. Grosdidier, A., V. Zoete, and O. Michielin. 2011. Fast docking using the CHARMM force field with EADock DSS. *J. Comput. Chem.* 32:2149–2159.

53. Grosdidier, A., V. Zoete, and O. Michielin. 2011. SwissDock, a protein-small molecule docking web service based on EADock DSS. *Nucleic Acids Res.* 39:W270–W277.

54. Pevzner, Y., E. Frugier, …, H. L. Woodcock. 2014. Fragment-based docking: development of the CHARMMing Web user interface as a platform for computer-aided drug design. *J. Chem. Inf. Model.* 54:2612–2620.

55. Jones, G., P. Willett, …, R. Taylor. 1997. Development and validation of a genetic algorithm for flexible docking. *J. Mol. Biol.* 267:727–748.

56. Österberg, F., G. M. Morris, …, D. S. Goodsell. 2002. Automated docking to multiple target structures: incorporation of protein mobility and structural water heterogeneity in AutoDock. *Proteins.* 46:34–40.

57. Repasky, M. P., M. Shelley, and R. A. Friesner. 2007. Flexible ligand docking with Glide. *Curr. Protoc. Bioinformatics.* Chapter 8:Unit 8.12.

58. Zhang, N., and H. Zhao. 2016. Enriching screening libraries with bioactive fragment space. *Bioorg. Med. Chem. Lett.* 26:3594–3597.

59. Ruiz-Carmona, S., D. Alvarez-Garcia, …, S. D. Morley. 2014. rDock: a fast, versatile and open source program for docking ligands to proteins and nucleic acids. *PLoS Comput. Biol.* 10:e1003571.

60. Morris, G. M., R. Huey, …, A. J. Olson. 2009. AutoDock4 and AutoDockTools4: automated docking with selective receptor flexibility. *J. Comput. Chem.* 30:2785–2791.

61. Allen, W. J., T. E. Balius, …, R. C. Rizzo. 2015. DOCK 6: impact of new features and current docking performance. *J. Comput. Chem.* 36:1132–1156.

62. Jain, A. N. 2007. Surflex-Dock 2.1: robust performance from ligand energetic modeling, ring flexibility, and knowledge-based search. *J. Comput. Aided Mol. Des.* 21:281–306.

63. Majeux, N., M. Scarsi, and A. Caflisch. 2001. Efficient electrostatic solvation model for protein-fragment docking. *Proteins.* 42:256–268.

64. Majeux, N., M. Scarsi, …, A. Caflisch. 1999. Exhaustive docking of molecular fragments with electrostatic solvation. *Proteins.* 37:88–105.

65. Lagarde, N., A. Carbone, and S. Sacquin-Mora. 2018. Hidden partners: using cross-docking calculations to predict binding sites for proteins with multiple interactions. *Proteins.* 86:723–737.

66. Kynast, P., P. Derreumaux, and B. Strodel. 2016. Evaluation of the coarse-grained OPEP force field for protein-protein docking. *BMC Biophys.* 9:4.

67. Wang, Z., H. Sun, …, T. Hou. 2016. Comprehensive evaluation of ten docking programs on a diverse set of protein-ligand complexes: the prediction accuracy of sampling power and scoring power. *Phys. Chem. Chem. Phys.* 18:12964–12975.

68. Pagadala, N. S., K. Syed, and J. Tuszynski. 2017. Software for molecular docking: a review. *Biophys. Rev.* 9:91–102.

69. Chaput, L., and L. Mouawad. 2017. Efficient conformational sampling and weak scoring in docking programs? Strategy of the wisdom of crowds. *J. Cheminform.* 9:37.

70. Athanasiou, C., S. Vasilakaki, …, Z. Cournia. 2018. Using physics-based pose predictions and free energy perturbation calculations to predict binding poses and relative binding affinities for FXR ligands in the D3R Grand Challenge 2. *J. Comput. Aided Mol. Des.* 32:21–44.

71. Gkeka, P., S. Eleftheratos, …, Z. Cournia. 2013. Free energy calculations reveal the origin of binding preference for aminoadamantane blockers of influenza A/M2TM pore. *J. Chem. Theory Comput.* 9:1272–1281.

72. Radom, F., A. Plückthun, and E. Paci. 2018. Assessment of ab initio models of protein complexes by molecular dynamics. *PLoS Comput. Biol.* 14:e1006182.

73. Tamamis, P., and C. A. Floudas. 2014. Elucidating a key anti-HIV-1 and cancer-associated axis: the structure of CCL5 (Rantes) in complex with CCR5. *Sci. Rep.* 4:5447.

74. Tamamis, P., and C. A. Floudas. 2014. Molecular recognition of CCR5 by an HIV-1 gp120 V3 loop. *PLoS One.* 9:e95767.

75. Tamamis, P., C. A. Kieslich, …, G. Archontis. 2014. Insights into the mechanism of C5aR inhibition by PMX53 via implicit solvent molecular dynamics simulations and docking. *BMC Biophys.* 7:5.

76. Tamamis, P., and C. A. Floudas. 2013. Molecular recognition of CXCR4 by a dual tropic HIV-1 gp120 V3 loop. *Biophys. J.* 105:1502–1514.

77. Renault, P., M. Louet, …, N. Floquet. 2019. Molecular dynamics simulations of the allosteric modulation of the adenosine A2A receptor by a mini-G protein. *Sci. Rep.* 9:5495.

78. Dror, R. O., H. F. Green, …, D. E. Shaw. 2013. Structural basis for modulation of a G-protein-coupled receptor by allosteric drugs. *Nature.* 503:295–299.

79. Lückmann, M., M. Trauelsen, …, T. M. Frimurer. 2019. Molecular dynamics-guided discovery of an ago-allosteric modulator for GPR40/FFAR1. *Proc. Natl. Acad. Sci. USA.* 116:7123–7128.

80. Denisov, I. G., Y. V. Grinkova, …, S. G. Sligar. 2019. Allosteric interactions in human cytochrome P450 CYP3A4: the role of phenylalanine 213. *Biochemistry.* 58:1411–1422.

81. Thayer, K. M., B. Lakhani, and D. L. Beveridge. 2017. Molecular dynamics-markov state model of protein ligand binding and allostery in CRIB-PDZ: conformational selection and induced fit. *J. Phys. Chem. B.* 121:5509–5514.

82. Stetz, G., and G. M. Verkhivker. 2015. Dancing through life: molecular dynamics simulations and network-centric modeling of allosteric mechanisms in Hsp70 and Hsp110 chaperone proteins. *PLoS One.* 10:e0143752.

83. Kasahara, K., I. Fukuda, and H. Nakamura. 2014. A novel approach of dynamic cross correlation analysis on molecular dynamics simulations and its application to Ets1 dimer-DNA complex. *PLoS One.* 9:e112419.

84. Gkeka, P., A. Papafotika, …, Z. Cournia. 2015. Exploring a non-ATP pocket for potential allosteric modulation of PI3Kα. *J. Phys. Chem. B.* 119:1002–1016.

85. Vainio, M. J., J. S. Puranen, and M. S. Johnson. 2009. ShaEP: molecular overlay based on shape and electrostatic potential. *J. Chem. Inf. Model.* 49:492–502.

86. Huang, J., and A. D. MacKerell, Jr. 2013. CHARMM36 all-atom additive protein force field: validation based on comparison to NMR data. *J. Comput. Chem.* 34:2135–2145.

87. Vanommeslaeghe, K., E. Hatcher, …, A. D. Mackerell, Jr. 2010. CHARMM general force field: a force field for drug-like molecules compatible with the CHARMM all-atom additive biological force fields. *J. Comput. Chem.* 31:671–690.

88. Huggins, D. J., and B. Tidor. 2011. Systematic placement of structural water molecules for improved scoring of protein-ligand interactions. *Protein Eng. Des. Sel.* 24:777–789.

89. Orr, A. A., M. M. Wördehoff, …, P. Tamamis. 2016. Uncovering the binding and specificity of β-Wrapins for Amyloid-β and α-Synuclein. *J. Phys. Chem. B.* 120:12781–12794.

90. Orr, A. A., H. Shaykhalishahi, …, P. Tamamis. 2018. Elucidating the multi-targeted anti-amyloid activity and enhanced islet amyloid polypeptide binding of β-wrapins. *Comput. Chem. Eng.* 116:322–332.

91. Im, W., M. S. Lee, and C. L. Brooks, III. 2003. Generalized born model with a simple smoothing function. *J. Comput. Chem.* 24:1691–1702.

92. Knight, J. L., and C. L. Brooks, III. 2011. Surveying implicit solvent models for estimating small molecule absolute hydration free energies. *J. Comput. Chem.* 32:2909–2923.

93. Lin, L. N., J. Li, …, R. M. Weis. 1994. The serine receptor of bacterial chemotaxis exhibits half-site saturation for serine binding. *Biochemistry.* 33:6564–6570.

94. Iwama, T., I. Kawagishi, …, Y. Imae. 1995. In vivo sulfhydryl modification of the ligand-binding site of Tsr, the *Escherichia coli* serine chemoreceptor. *J. Bacteriol.* 177:2218–2221.

Supplemental Information

Molecular Mechanism for Attractant Signaling to DHMA by *E. coli* Tsr

Asuka A. Orr, Jingyun Yang, Nitesh Sule, Ravi Chawla, Kenneth G. Hull, Mingzhao Zhu, Daniel Romo, Pushkar P. Lele, Arul Jayaraman, Michael D. Manson, and Phanourios Tamamis

Molecular Mechanism for Attractant Signaling to DHMA by *E. coli* Tsr

Supporting Material

Asuka A. Orr[1], Jingyun Yang[1], Nitesh Sule[1], Ravi Chawla[1], Kenneth G. Hull[2], Mingzhao Zhu[2], Daniel Romo[2], Pushkar P. Lele[1], Arul Jayaraman[1], Michael D. Manson[3*], Phanourios Tamamis[1*]

[1]Artie McFerrin Department of Chemical Engineering, Texas A&M University, College Station, TX 77843, USA

[2]Department of Chemistry & Biochemistry and CPRIT Synthesis and Drug-Lead Discovery Laboratory, Baylor University, Waco, TX 76798, USA

[3]Department of Biology, Texas A&M University, College Station, TX 77843, USA

*Correspondence: mike@bio.tamu.edu, tamamis@tamu.edu

Tel.: +1-979-862-1610

Fax: +1-979-845-6446

Supporting computational methods

Docking (*S*)-DHMA to pTsr. We performed a nearly exhaustive search of all binding modes of (*S*)-DHMA in complex with *E. coli* Tsr, which aimed to predict the most energetically favorable binding mode through an in-house developed docking-refinement protocol (1-6) for use as the initial structure for subsequent MD simulations and detailed analysis. The protocol can be divided into the following stages: (1) the initial positioning of the ligand within the receptor binding pocket, based on available experimental data; (2) multiple short MD docking simulations nearly exhaustively searching binding conformations of the ligand within the receptor binding pocket, with the ligand constrained to the binding pocket though harmonic and quartic spherical potentials and the binding pocket of the receptor unconstrained; (3) interaction energy calculations evaluating the resulting binding conformations to select the most probable binding modes generated by the short docking simulations; and (4) explicit-solvent MD simulations and physical-chemistry based free-energy calculations are employed to identify the most favorable binding mode of the ligand:receptor complex (Figure S1). The docking-refinement protocol was first developed and executed to study and compare the binding of agonist and antagonist compounds to the mouse aryl hydrocarbon receptor (2). Since its debut, we have applied the docking-refinement protocol to detect the most energetically favorable binding modes of flavonoids binding to the human aryl hydrocarbon receptor (3,6), compound inhibitor binding to C3c (4), compounds binding to the human COUP-TF1 and COUP-TF2 (5), as well as (*R*)-DHMA binding to *E. coli* Tsr (1), the latter of which is also investigated in the current study.

Here, we employed the in-house docking-refinement protocol (1) to determine the most energetically favorable binding mode of (*S*)-DHMA binding to pTsr. In line with the docking-refinement protocol and our previous study of (*R*)-DHMA binding to pTsr (1), the initial placement

of (*S*)-DHMA into the binding site of *E. coli* pTsr was guided by the experimentally resolved ligand serine bound in Chain A of the crystal structure of the serine:pTsr complex (PDB ID: 3ATP (7)) using the ShaEP algorithm (8), as previous experimental studies (9) showed that DHMA shares the same binding pocket as serine and that attractant chemotaxis to DHMA requires an intact serine-binding site in Tsr. Subsequently, short docking simulations were introduced to search binding modes of the (*S*)-DHMA:pTsr complex (Figure S1, cyan block). In the short docking simulations, 20 independent runs were performed, in which 200 steps of 2 ps simulations were conducted. For each of the 200 steps, the ligand was rotated about a randomly generated axis, followed by a 2 ps MD simulation and energetic minimization; data were saved for subsequent evaluation (Figure S1, cyan block). The result was 4000 saved binding modes of the (*S*)-DHMA:pTsr complex per docking simulation. Throughout the duration of the short docking simulations, (*S*)-DHMA was constrained in the binding site using quartic and harmonic spherical potentials through the MMFP module of CHARMM (10) (Figure S1, blue block). The binding pocket residues (56, 59-76, 81-94, 130-144, 147-162, 59'-76' – where residues marked with a prime symbol (') belong to the protein subunit of the pTsr dimer with fewer interacting residues (considered to be the minority side) were unconstrained and flexible. The absence of constraints on the binding pocket residues aimed to facilitate the ability of the residues to adopt to the different binding modes of the ligand generated through random rotations (Figure S1, yellow block, pocket encircled by red dotted lines). Five separate sets of docking simulations, or docking systems, were introduced to explore the possible binding modes of (*S*)-DHMA. Four docking systems utilized harmonic spherical potentials, and one system utilized a quartic spherical potential (Figure S1, orange blocks within blue block). The quartic spherical potential introduces an energetic well away from the center of the spherical potential and thus encourages the ligand to move away from its

initial position. The independent use of both quartic and harmonic spherical potentials allowed for the exploration of binding modes both away from (quartic) and in proximity to (harmonic) the initial positioning of the ligand (see Eq. 2 of ref. (1)). From each of the docking simulation systems, the three binding modes with the lowest interaction energy were selected for further investigation resulting in 15 binding modes (Figure S1, green and red blocks). The 15 binding modes of the (*S*)-DHMA:pTsr complex were investigated through 20 ns explicit-solvent MD simulations to refine the ligand:receptor structures, optimize intermolecular interactions, determine the structural stability of the selected binding modes, and determine the most energetically favorable binding modes. All MD simulations were performed in explicit solvent using CHARMM (10) and CHARMM36 topologies and parameters (11) with periodic boundary conditions. Topologies and parameters for (*S*)-DHMA were obtained from CGENFF (12). The energetic favorability of the binding modes was assessed using MM-GBSA association free-energy calculations (13), in line with our previous study on (*R*)-DHMA binding to pTsr (1). The predicted binding modes of (*S*)-DHMA with the most favorable average MM-GBSA association free-energy were compared with all other binding modes to ensure that all other binding modes were far less energetically favorable than the predicted mode. Binding modes with similar association free-energies to the predicted binding mode were visually inspected to verify that their structures were similar to the structure of the most energetically favorable binding mode (1). The structure resulting in the most energetically favorable binding mode was used as the initial structure of the (*S*)-DHMA:pTsr complex used for the subsequent five replicate 100 ns MD simulations described in the main text.

Investigating (*R*)-DHMA and (*S*)-DHMA in complex with pTsr using multiple MD simulations. From the 15 binding modes of (*R*)-DHMA:pTsr and the 15 binding modes of the (*S*)-DHMA:pTsr, we selected the most energetically favorable binding modes of (*R*)- and (*S*)-DHMA

in complex with pTsr for further investigation. Using the structures resulting in the most energetically favorable binding modes of (*R*)- and (*S*)-DHMA in complex with pTsr as initial structures, we performed five independent replicate 100 ns MD simulations of (*R*)- and (*S*)-DHMA in complex with pTsr with simulation snapshots extracted every 20 ps. Prior to the production run, the structures were equilibrated in two stages. In the first equilibration stage, the system was equilibrated using a 1 ns explicit solvent MD simulation, in which the heavy atoms of the ligand and Tsr backbone atoms were constrained with a harmonic force constant of $1.0 \text{ kcal/(mol·Å}^2)$ and the Tsr side chain atoms were constrained with a harmonic force constant of $0.1 \text{ kcal/(mol·Å}^2)$. In the second stage, all constraints on the Tsr protein were released and the ligand was lightly constrained with a harmonic force constant of $0.5 \text{ kcal/(mol·Å}^2)$. Upon completion of the 100 ns MD simulations, we performed energetic and structural analyses on the 25,000 simulation snapshots resulting from the five replicate 100 ns MD simulations for each enantiomer.

To determine the presence of water-mediated interactions and their role in (*R*)- and (*S*)-DHMA binding, we developed FORTRAN programs to detect pTsr residues interacting with the enantiomers through water. A hydrogen bond donor/acceptor atom of a pTsr residue was considered to be interacting with (*R*)- or (*S*)-DHMA if (1) any of their hydrogen bond donor/acceptor atoms were within 3.5 Å of the oxygen of the same water molecule and (2) the angle between the vector from the oxygen of the water molecule to the atom of the given pTsr residue and the vector from the oxygen of the water molecule to the atom (*R*)- or (*S*)-DHMA was less than 150° (14).

To investigate and potentially differentiate the key interactions associated with the binding of (*R*)-DHMA and (*S*)-DHMA, we calculated the average interaction-free-energies between each pTsr residue and both ligands within their respective simulation snapshots using the MM-GBSA

approximation (13). The per-pTsr residue interaction-free-energies for each of the 5 replicate 100 ns MD simulation production run were calculated for their full duration, in increments of 200 ps, using CHARMM (10), Wordom (15), and in-house FORTRAN programs. The interaction-free-energies between the ligand and each pTsr residue were calculated using Eq. 1, as in refs. (1-5,16-18).

$$\Delta G_{RL}^{\text{inte}} = \sum_{i \in R} \sum_{j \in L} \left(E_{ij}^{\text{Elec}} + E_{ij}^{\text{GB}} \right) + \sum_{i \in R} \sum_{j \in L} E_{ij}^{\text{vdW}} + \gamma \sum_{i \in R,L} \Delta(\text{SASA}_i)$$

Eq. 1

The polar component of the interaction-free-energy between a pTsr residue, R, and the ligand, L, is represented by the sum of the electrostatic, E_{ij}^{Elec}, and polar solvation, E_{ij}^{GB}, free-energy terms. The non-polar component of the interaction-free-energy between R and L is represented by the sum of the Van der Waals, E_{ij}^{vdW}, and non-polar solvation, $\gamma \cdot \text{SASA}$, free-energy terms.

The electrostatic interaction contribution represents the interaction between residue R and ligand L, and the polar solvation contribution represents the interaction of residue R with the solvent polarization potential induced by L. The van der Waals contribution represents the non-polar interaction between residue R and ligand L, and the non-polar solvation contribution represents the non-polar interactions with the surrounding solvent and cavity contributions due to binding. The solvation terms were determined using the GBSW generalized-Born model (19). The interaction free-energy-calculations were performed using a non-polar surface tension coefficient, γ, of 0.03 kcal/(molÅ²) (20).

The per-residue interaction-free-energy between pTsr residues and the two ligands, (R)- and (S)-DHMA, were independently averaged over the number of simulation snapshots and number of replicate MD simulations (five MD simulations). The energetically favorable per-residue interaction-free-energy values between pTsr residues and the two ligands, defined as those with

energy values less than -1 kcal/mol, are decomposed into polar and non-polar contributions and are presented in Figure 2.

Investigating serine bound and apo pTsr. We performed five 100 ns MD simulations of serine in complex with pTsr and two 100 ns MD simulations of an unbound (apo) Tsr. The simulations were performed as controls to ensure that the observed piston-like push-down of α-helix 4 is not an artifact of the MD simulations and is observed in simulations of a known Tsr chemoattractant (serine) and not observed in the apo pTsr. The starting structure of the serine:Tsr complex corresponded to the crystal structure of pTsr bound by serine (PDB ID: 3ATP) (7) with the bound serine in Chain B removed. While Tsr contains two symmetric serine-binding sites, only one functional site suffices for serine sensing (21,22). Thus, for a fair comparison with the binding of (*R*)-DHMA and (*S*)-DHMA to pTsr, the second bound serine within the crystal structure with disordered electron density (7) was removed. The starting structure of the apo pTsr corresponded to the crystal structure of pTsr bound by serine (PDB ID: 3ATP) (7) with both bound serine ligands removed. The simulation setup and parameters were the same as those used to investigate the binding of (*R*)- and (*S*)-DHMA described above and in ref. (1). Upon completion of the 100 ns MD simulations, we calculated the projected lengths of α-helix 4 per simulation snapshot for each simulation run as described in *Investigating piston-like motions in pTsr caused by binding of (R)-DHMA and (S)-DHMA*. The projected lengths are shown in Figure S3.

Data S1. Coordinates of (*R*)- and (*S*)-DHMA in complex with pTsr from the 100-ns MD simulations provided in PDB format. The 25 ns, 50 ns, 75 ns, and 100 ns MD coordinates of the MD simulated (*R*)-DHMA:Tsr complex and the MD simulated (*S*)-DHMA:Tsr complex are provided as *Supporting Material* in PDB format. The structures are aligned with respect to the backbone of the entire modeled pTsr. The correspondence of PDB files and the number of the MD simulation from which the coordinates originate are shown in the table.

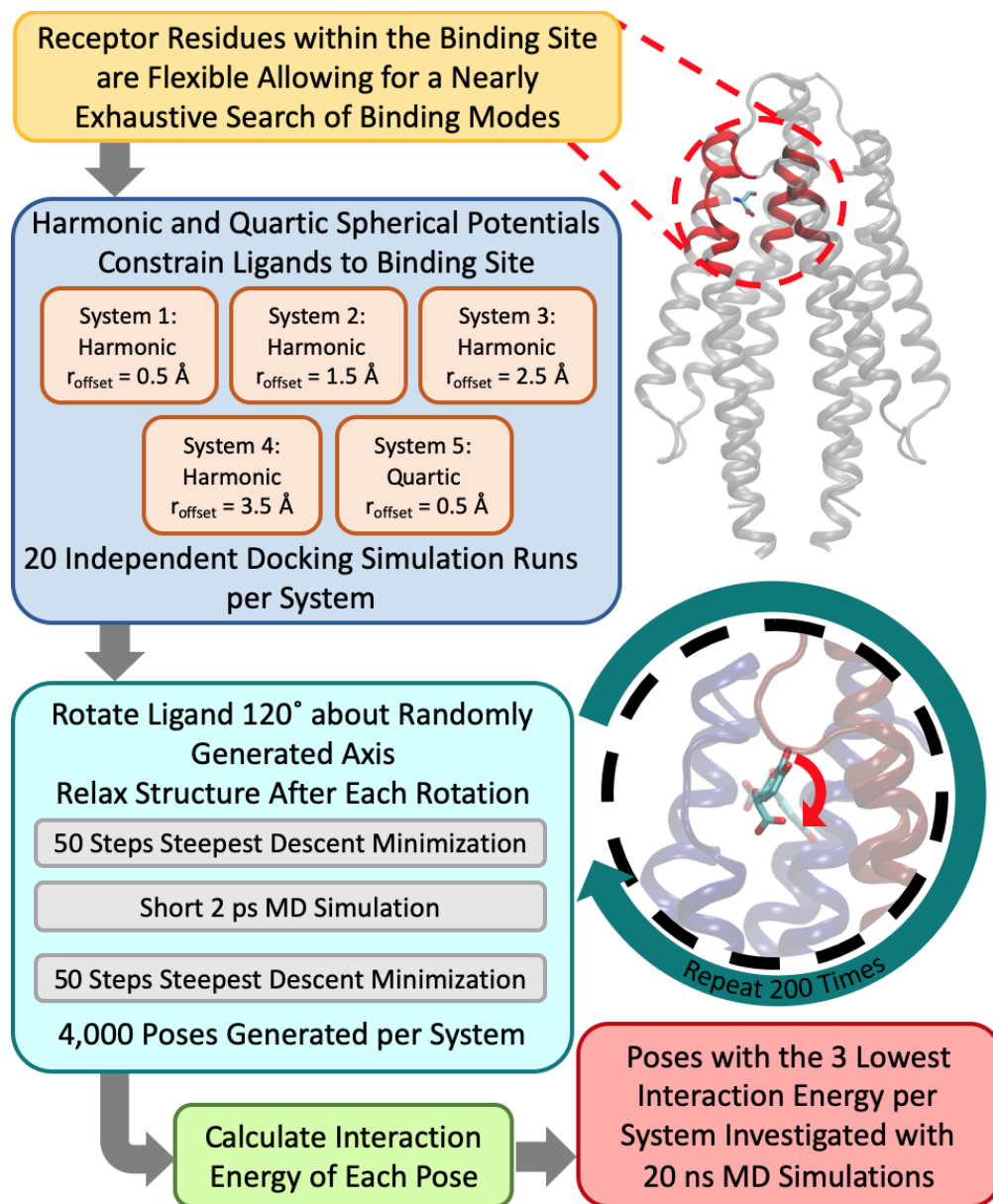| PDB file	Complex	Simulation
coordinates.rdhma1.pdb	(*R*)-DHMA	1
coordinates.rdhma2.pdb	(*R*)-DHMA	2
coordinates.rdhma3.pdb	(*R*)-DHMA	3
coordinates.rdhma4.pdb	(*R*)-DHMA	4
coordinates.rdhma5.pdb	(*R*)-DHMA	5
coordinates.sdhma1.pdb	(*S*)-DHMA	1
coordinates.sdhma2.pdb	(*S*)-DHMA	2
coordinates.sdhma3.pdb	(*S*)-DHMA	3
coordinates.sdhma4.pdb	(*S*)-DHMA	4
coordinates.sdhma5.pdb	(*S*)-DHMA	5

Figure S1. Workflow for the docking refinement protocol used to obtain the most energetically favorable binding mode of (*S*)-and (*R*)-DHMA in complex with pTsr, which were used as initial structures for the five replicate multi-ns MD simulations.
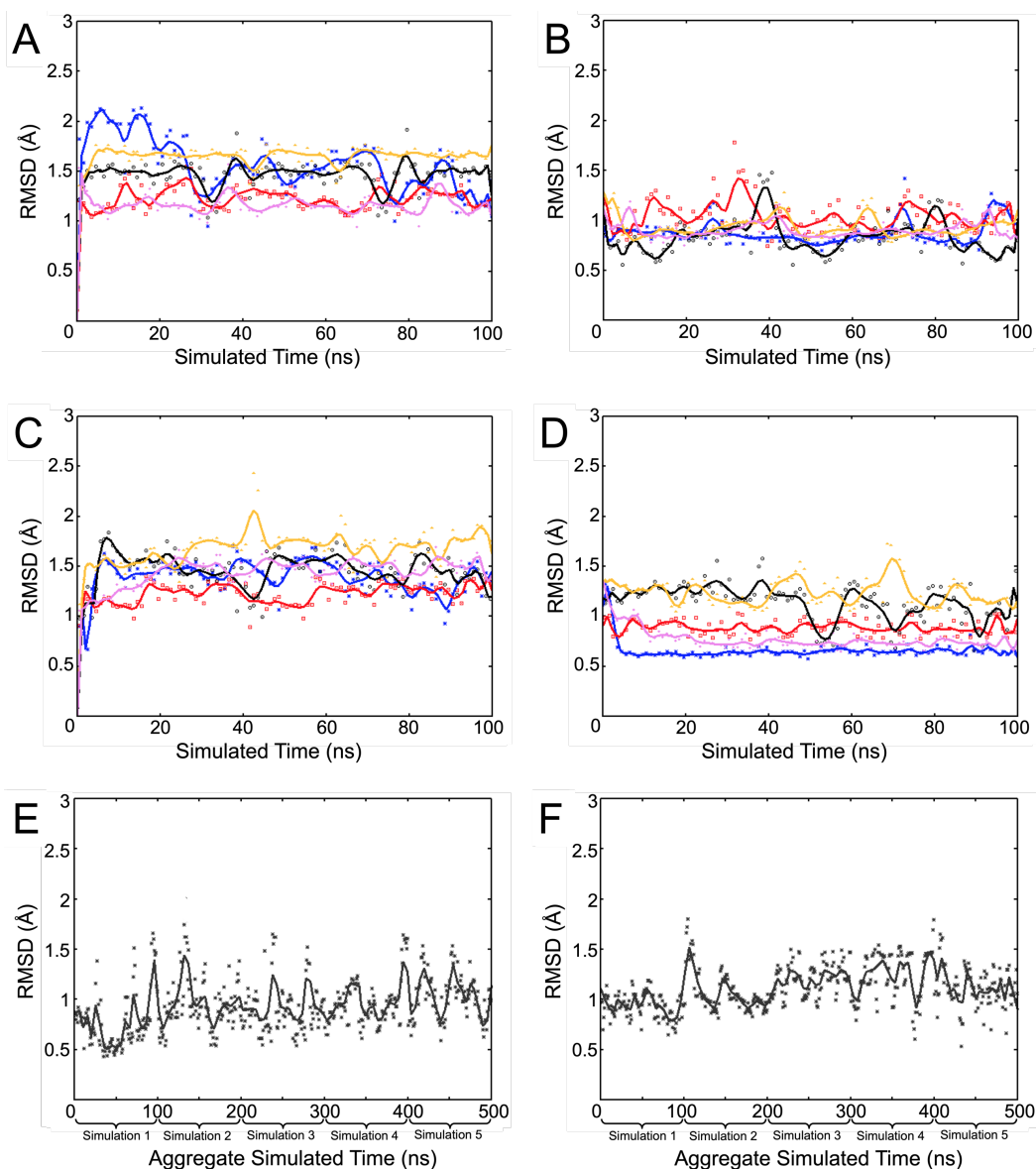
Figure S2. RMSD (in Å) of (A,B) (*R*)-DHMA and (C,D) (*S*)-DHMA with respect to (A,C) their respective initial structures and (B,D) their respective average structures throughout independent 100 ns simulations. RMSD (in Å) of (E) (*R*)-DHMA and (F) (*S*)-DHMA with respect to their respective average structures throughout their five combined 100 ns simulations. The plotted RMSD values correspond to values extracted every 1 ns. The plotted RMSD values correspond to values extracted every 1 ns. Solid lines correspond to Bezier curves fitted to RMSD values extracted every 0.1 ns. Blue, red, black, yellow, and pink data points and lines correspond to data extracted from the simulations starting from the first, second, third binding mode differing from the lowest association free-energy binding mode for each of the complexes.
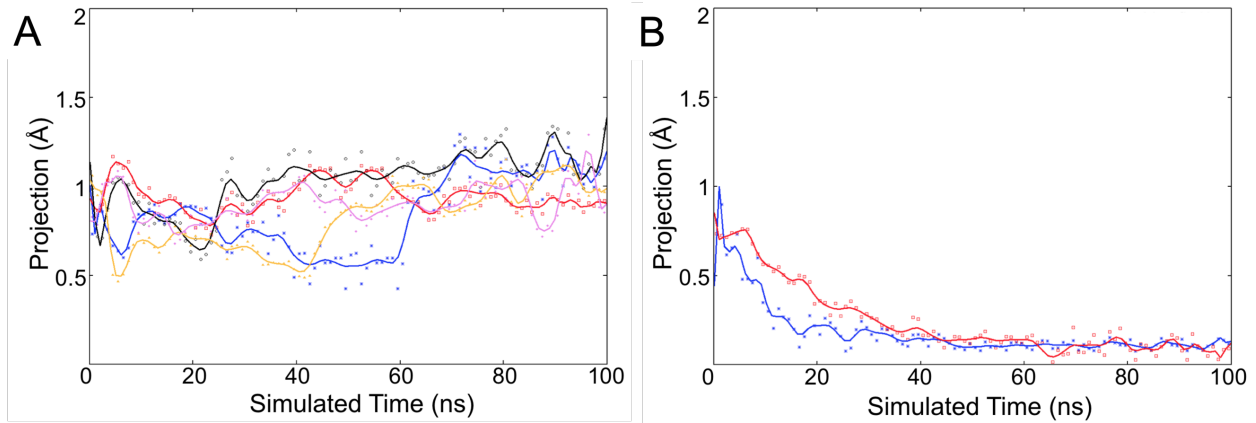
Figure S3. Vector projections showing the normalized magnitude of piston-like motions (in Å) within α-helix 4 of pTsr (A) bound to serine and (B) unbound with respect to the simulated time (in ns). The projection values plotted correspond to projected lengths, p_i, calculated using Eq. 2 and extracted every 1 ns. Solid lines correspond to Bezier curves fitted to projected lengths extracted every 0.1 ns. (A) Blue, red, black, yellow, and pink data points and lines correspond to data extracted from the first, second, third, fourth, and fifth simulations, respectively. (B) Blue and red data points and lines correspond to data extracted from the first and second simulations, respectively.

Supporting experimental material

Resolution and isolation of DHMA enantiomers. ^{1}H NMR data were recorded at 25 °C using an INOVA-500 equipped with Prodigy Cold Probe NMR at 500 MHz. Chemical shifts are reported in ppm using the solvent resonance as the internal standard (^{1}H NMR CD$_3$C(O)CD$_3$:δ 2.05 ppm). Data are reported as follows: chemical shift, multiplicity (s = singlet, d = doublet, t = triplet, q = quartet, bs = broad singlet, m = multiplet, or any combination of these), coupling constants (Hz) and integration. Low Resolution Mass Spectrometry (LRMS) analysis was obtained using an Amazon ion-trap mass spectrometer utilizing Electrospray Ionization (ESI), and the data are reported as m/z (relative intensity). Optical rotations were recorded at 589 nm employing a 25 mm cell. Specific rotations $[\alpha]_D^{20}$, are reported in degree mL/(g•dm) at the specific temperature. HPLC separations were run using an Agilent 1200 series (analytical) or an Agilent 1260 Infinity system (preparative). Preparative reversed-phase HPLC was done using a Gemini 5 micron C18 110A (100 x 21.2 mm) AXIA column. Analytical chiral stationary phase HPLC separations were run on a CHIRALPAK ID-3 (150 x 4.6 mm I.D., 3 micron) column, and preparative chiral stationary phase HPLC separations were run on a CHIRALPAK ID (250 x 20 mm I.D., 5 micron) column. The Amano Lipase PS was purchased from Sigma Aldrich. THF and MTBE were used in the kinetic resolution without drying the solvents.

Separation of (*R*)-DHMA and (*S*)-DHMA. Analytical separation was achieved with a CHIRALPAK ID-3 (150 x 4.6 mm I.D., 3 micron) column using methanol/water (10:90) and 0.1% formic acid as the mobile phase (0.6 ml/min flow rate). On the analytical HPLC column, the enantiomers of DHMA had retention times of 4.0 and 5.9 min, and we assigned the (*R*) and (*S*) configuration, respectively (Figure S4).
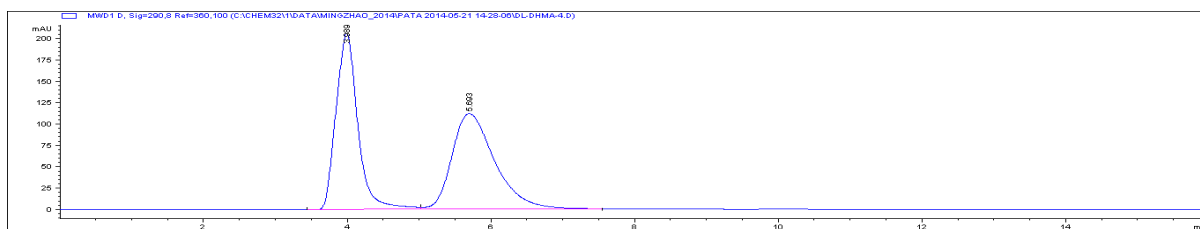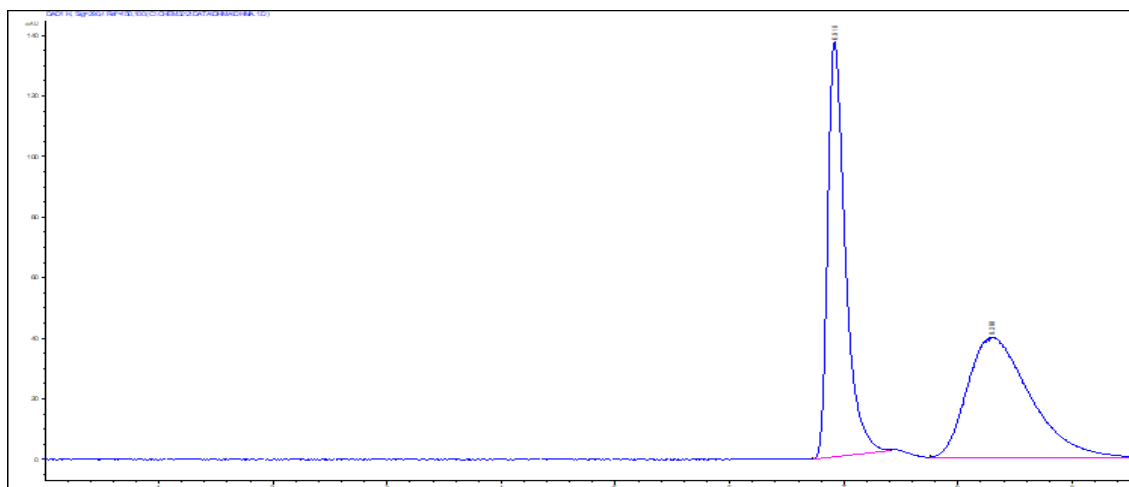
Figure S4. Chromatogram of racemic DHMA on the chiral analytical column (DHMA 3 mg/mL in MeOH, 4 μL injection).

Preparative separation was achieved with a CHIRALPAK ID (250 x 20 mm I.D., 5 micron) column using methanol/water (20:80) and 0.1% formic acid as the mobile phase (10 ml/min flow rate). On the preparative HPLC column, the enantiomers of DHMA had retention times of 6.9 and 8.3 min., and we assigned the (*R*) and (*S*) configuration, respectively (Figure S5).
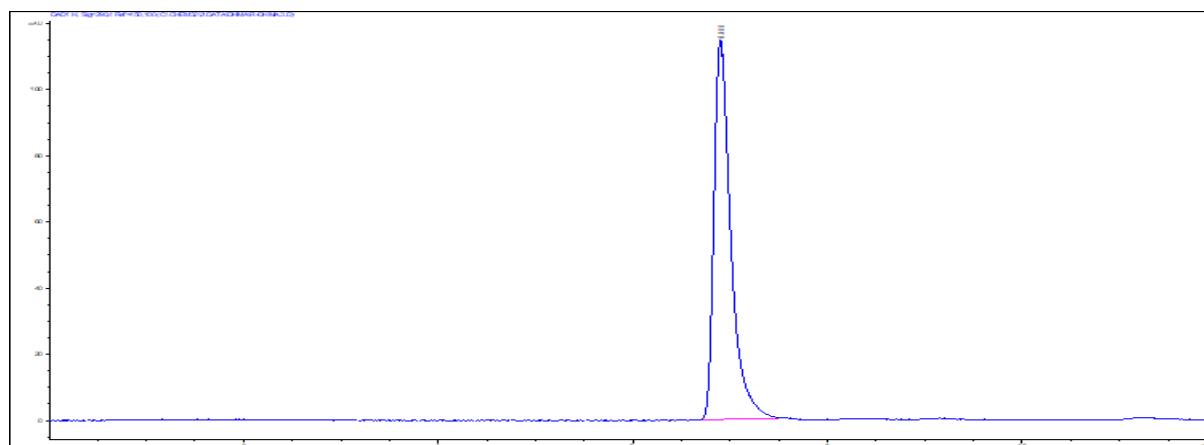


```
Signal 1: DAD1 H, Sig=290,4 Ref=450,100

Peak RetTime  Type   Width     Area      Area
 #    [min]          [min]    [mAU*s]     %
----|-------|------|-------|----------|--------|
  1   6.919  BB    0.1381  1467.42883  49.3925
  2   8.298  BB    0.4504  1503.52576  50.6075
```

Figure S5. Chromatogram of racemic DHMA on the chiral preparative column (DHMA 10 mg/mL in MeOH, 120 μL injection).

(*R*)-DHMA and (*S*)-DHMA separated by preparative HPLC. A solution of racemic DHMA (20 mg, 10 mg/mL) was separated as described above with 4 injections (~ 500 μL each) on the preparative column. The fractions containing each peak were combined, concentrated, then freeze-dried on a lyophilizer overnight to provide 9 mg of (*R*)-DHMA (RT = 6.9 min) and 8 mg of (*S*)-DHMA (RT = 8.3 min).

(*R*)-DHMA All spectral data for this compound were consistent with those previously reported for racemic DHMA (Sigma-Aldrich and BioRad), > 98% ee by HPLC analysis, Optical rotation [α] – 209.9 (*c* 0.465, MeOH) (Figure S6).


```
Signal 1: DAD1 H, Sig=290,4 Ref=450,100

Peak RetTime  Type   Width     Area        Area
 #    [min]          [min]    [mAU*s]       %
----|-------|------|-------|----------|--------|
  1   6.900  BB     0.1513 1379.70410 100.0000

Totals :                   1379.70410
```

Figure S6. Chromatogram of (*R*)-DHMA after separation by HPLC (chiral prep column, 5 mg/mL in MeOH, 150 μL injection).

(*S*)-DHMA All spectral data for this compound were consistent with those previously reported for racemic DHMA (Sigma-Aldrich and BioRad), 94% ee by HPLC analysis, optical rotation [α] + 195.2 (*c* 0.31, MeOH) (Figure S7).

Peak | RetTime | Type | Width | Area | Area
#	[min]		[min]	[mAU*s]	%
1	6.941	BB	0.1334	56.78226	2.7439
2	8.235	BB	0.4968	2012.60059	97.2561
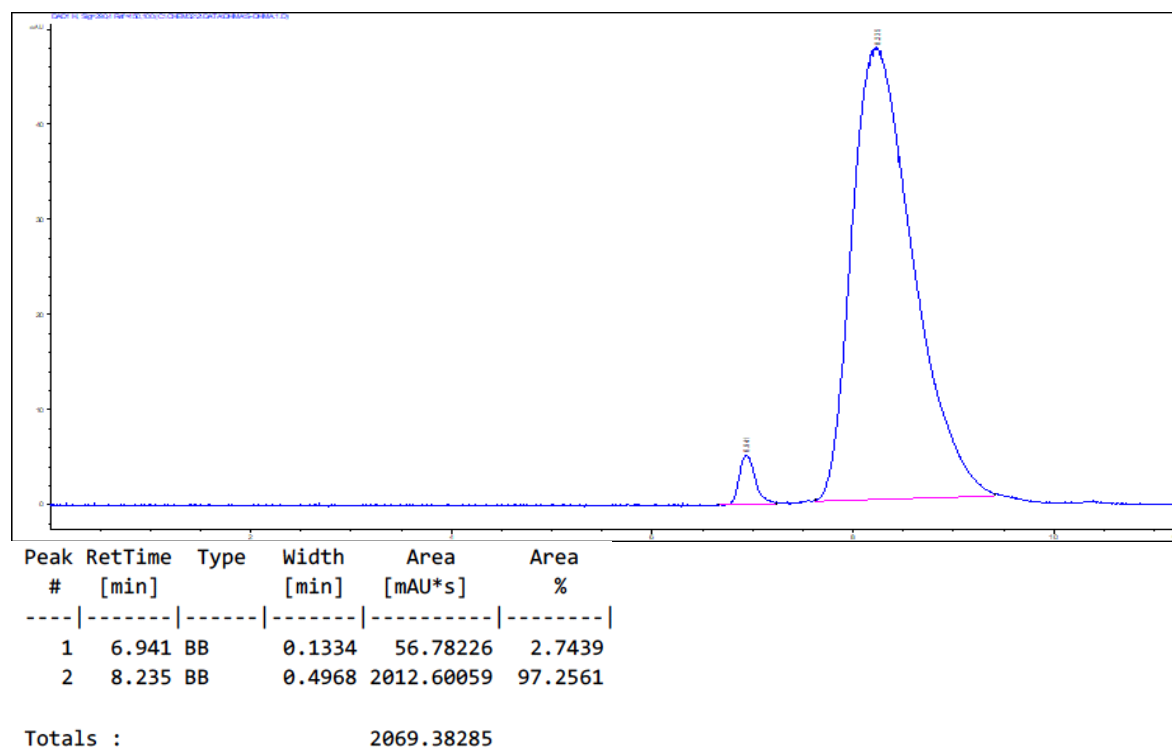
Totals :   2069.38285

Figure S7. Chromatogram of (*S*)-DHMA after separation by HPLC (chiral prep column, 5 mg/mL in MeOH, 120 μL injection).

Kinetic resolution of racemic DHMA, isolation of enriched (*R*)-DHMA 2 and acetate 3.

Amano Lipase PS (~ 5 mg) was added to a stirred solution of racemic DHMA (22 mg, 0.12 μmol, 1 equivalent) and vinyl acetate (300 mg, 3.49 mmol, 29 equiv) in methyl t-butyl ether/ THF (7:1, 2 ml). The resultant mixture was stirred at room temperature for 24 h. The reaction mixture was passed through a pad of celite, the pad was washed with 2 ml of THF, and the filtrate was concentrated. The crude mixture was purified by preparative reversed-phase HPLC using a Gemini 5 micron C18 110A (100 x 21.2 mm) AXIA column, gradient 5-95% CH_3CN/Water over 20 min.

Fractions containing each peak were freeze-dried on a lyophilizer overnight to yield unreacted (*R*)-DHMA **2** (RT = 5.1 min, 9 mg, 41% recovered yield) and acetate **3** (RT = 8.5 min., 10.3 mg, 40% yield) (Figure S8).
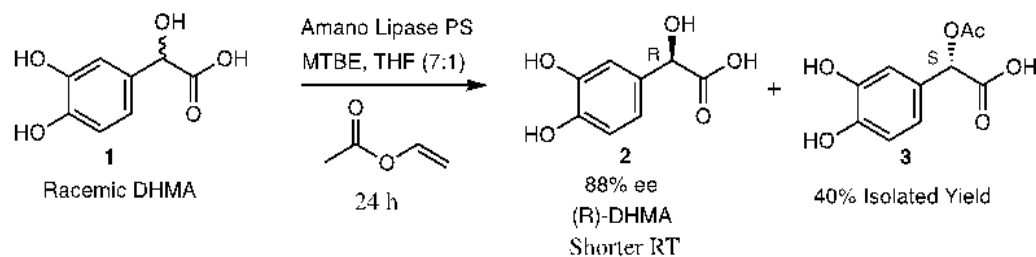

Figure S8. Reaction of racemic DHMA resulting in separated (*R*)-DHMA and reacted (*S*)-DHMA.

Recovered (*R*)-DHMA All spectral data for this compound was consistent with that previously reported for racemic DHMA (Sigma-Aldrich and BioRad), 88% ee by HPLC analysis (Figure S9).

Acetate 3 ^{1}H NMR (500 MHz, CD$_3$COCD$_3$) δ 6.97 (s, 1H), 6.90 - 6.72 (m, 2H), 5.68 (s, 1H), 2.08 (s, 3H); LRMS (ESI+) *m/z* calcd for C$_{10}$H$_9$O$_6$ [M − H]$^-$: 183.0; found: 183.1 (Figure S10).
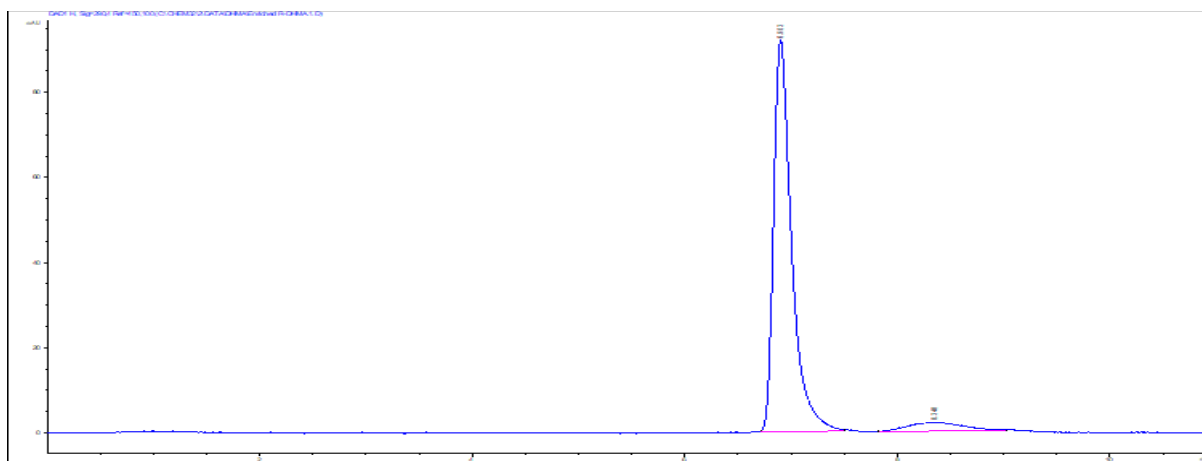
Signal 1: DAD1 H, Sig=290,4 Ref=450,100

```
Peak RetTime  Type   Width      Area      Area
 #    [min]          [min]    [mAU*s]       %
----|-------|------|-------|----------|--------|
  1   6.903 BB      0.1635 1084.72852  93.7527
  2   8.348 BB      0.4118   72.28207   6.2473

Totals :                    1157.01059
```

Figure S9. Chromatogram of highly enriched (*R*)-DHMA isolated after kinetic resolution by HPLC (Chiral prep column, 2 mg/mL in MeOH, 200 μL injection).
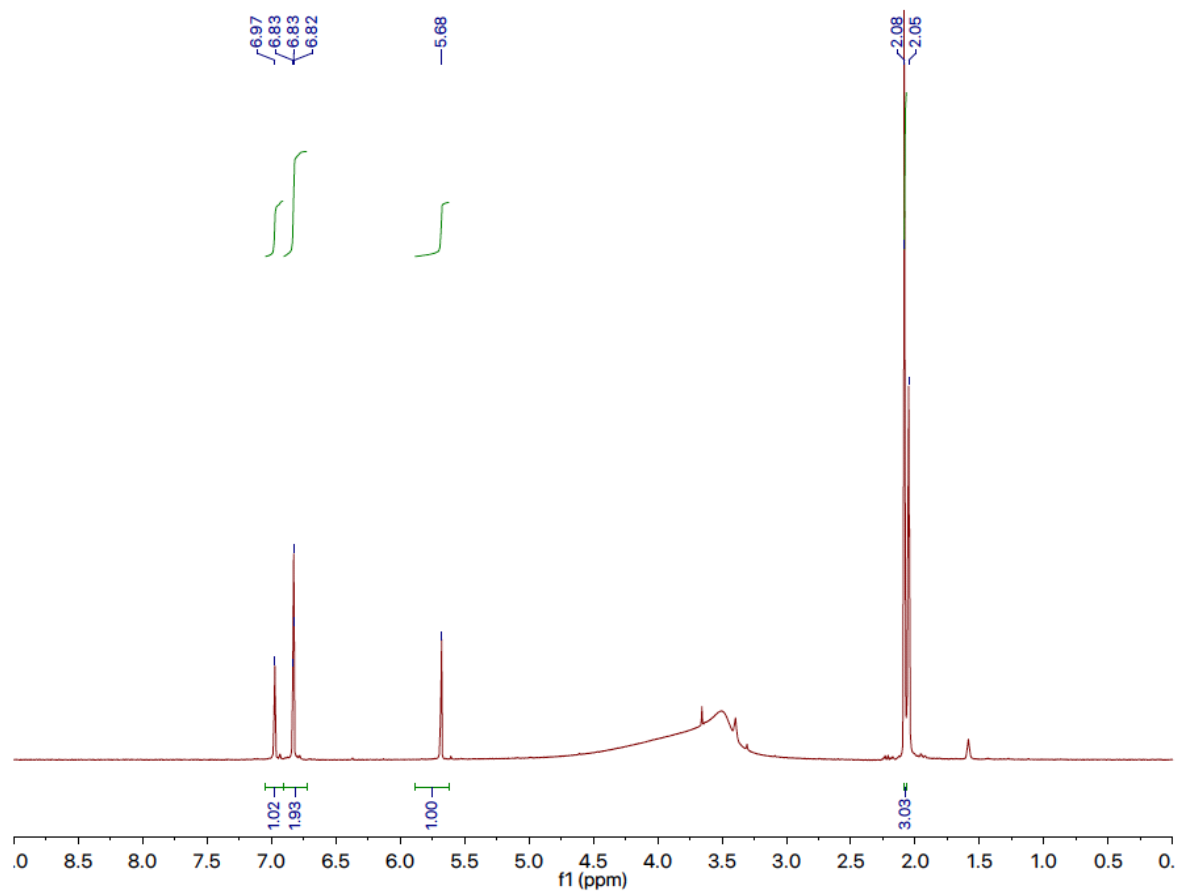
Figure S10. Acetate 3 ^{1}H NMR (500 MHz, CD$_3$COCD$_3$). Acetate 3 ^{1}H NMR (500 MHz, CD$_3$COCD$_3$) δ 6.97 (s, 1H), 6.90 - 6.72 (m, 2H), 5.68 (s, 1H), 2.08 (s, 3H).

Supporting References

(1) Orr, A. A., A. Jayaraman, and P. Tamamis. 2018. Molecular Modeling of Chemoreceptor: Ligand Interactions. Methods Mol. Biol. 1729:353-372.

(2) Jin, U. H., Y. Cheng, H. Park, L. A. Davidson, E. S. Callaway, R. S. Chapkin, A. Jayaraman, A. Asante, C. Allred, E. A. Weaver, S. Safe. 2017. Short chain fatty acids enhance aryl hydrocarbon (Ah) responsiveness in mouse colonocytes and Caco- 2 human colon cancer cells. Sci. Rep. 7(1):10163.

(3) Jin, U. H., H. Park, X. Li, L. A. Davidson, C. Allred, B. Patil, G. Jayaprakasha, A. A. Orr, L. Mao, R. S. Chapkin, A. Jayaraman, P. Tamamis, S. Safe. 2018. Structure-Dependent Modulation of Aryl Hydrocarbon Receptor-Mediated Activities by Flavonoids. Toxicol Sci. 164(1):205-217.

(4) Mohan, R. R., M. Wilson, R. D. Gorham Jr., R. E. S. Harrison, V. A. Morikis, C. A. Kieslich, A. A. Orr, A. V. Coley, P. Tamamis, D. Morikis. 2018. Virtual Screening of Chemical Compounds for Discovery of Complement C3 Ligands. A. C. S. Omega 3:6427–6438.

(5) Yoon, K., Chen, C. C., Liu, S., Orr, A. A., Barreto P. N., Tamamis, P., and Safe, S. 2019. Activation of COUP-TFI by a Novel Diindolymethane Derivative. Cells. 8(3): 220.

(6) Park, H., J. Un-Ho, A. A. Orr, S. P. Echegaray, L. A. Davidson, C. D. Allred, R. S. Chapkin, A. Jayaraman, K. Lee, P. Tamamis, and S. Safe. 2019. Isoflavones as Ah Receptor Agonists in Colon-Derived Cell Lines: Structure–Activity Relationships. Chem. Res. Toxicol. doi: 10.1021/acs.chemrestox.9b00352

(7) Tajima, H., K. Imada, M. Sakuma, F. Hattori, T. Nara, N. Kamo, M. Homma, and I. Kawagishi. 2011. Ligand specificity determined by differentially arranged common ligand-binding residues in bacterial amino acid chemoreceptors Tsr and Tar. J. Biol. Chem. 286(49):42200-42210.

(8) Vainio, M. J., J. S. Puranen, and M. S. Johnson. 2009. ShaEP: molecular overlay based on shape and electrostatic potential. J. Chem. Inf. Model. 49(2):492-502.

(9) Pasupuleti, S., N. Sule, W. B. Cohn, D. S. MacKenzie, A. Jayaraman, and M. D. Manson. 2014. Chemotaxis of *Escherichia coli* to norepinephrine (NE) requires conversion of NE to 3,4-dihydroxymandelic acid. J. Bacteriol. 196(23):3992-4000.

(10) Brooks, B. R., C. L. Brooks 3rd, A. D. Mackerell Jr., L. Nilsson, R. J. Petrella, B. Roux, Y. Won, G. Archontis, C. Bartels, S. Boresch, A. Caflisch, L. Caves, Q. Cui, A. R. Dinner, M. Feig, S. Fischer, J. Gao, M. Hodoscek, W. Im, K. Kuczera, T. Lazaridis, J. Ma, V. Ovchinnikov, E. Paci, R. W. Pastor, C. B. Post, J. Z. Pu, M. Schaefer, B. Tidor, R. M. Venable, H. L. Woodcock, X. Wu, W. Yang, D. M. York, and M. Karplus. 2009. CHARMM: the biomolecular simulation program. J. Comput. Chem. 30(10):1545-1614.

(11) Huang, J., and A. D. MacKerell Jr. 2013. CHARMM36 all-atom additive protein force field: validation based on comparison to NMR data. J Comput Chem. 34(25):2135-2145.

(12) Vanommeslaeghe, K., E. Hatcher, C. Acharya, S. Kundu, S. Zhong, J. Shim, E. Darian, O. Guvench, P. Lopes, I. Vorobyov, and A. D. Mackerell Jr. 2010. CHARMM general force field: A force field for drug-like molecules compatible with the CHARMM all-atom additive biological force fields. J Comput Chem. 31(4):671-690.

(13) Hayes, J. M., and G. Archontis. 2012. MM-GB(PB)SA Calculations of Protein-Ligand Binding Free Energies. Molecular Dynamics - Studies of Synthetic and Biological Macromolecules. L. Wang, editor. InTech, Southern Illinois University Carbondale, United States of America, pp. 171-190.

(14) Huggins, D. J., B. Tidor. 2011. Systematic placement of structural water molecules for improved scoring of protein-ligand interactions. Protein Eng Des Sel. (10):777-789.

(15) Seeber, M., A. Felline, F. Raimondi, S. Muff, R. Friedman, F. Rao, A. Caflisch, and F. Fanelli. 2011. Wordom: a use(R)-friendly program for the analysis of molecular structures, trajectories, and free energy surfaces. J. Comput. Chem. 32(6):1183-1194.

(16) Tamamis, P., C. A. Kieslich, G. V. Nikiforovich, T. M. Woodruff, D. Morikis, and G. Archontis. 2014. Insights into the mechanism of C5aR inhibition by PMX53 via implicit solvent molecular dynamics simulations and docking. BMC Biophys. 7:5.

(17) Orr, A. A., M. M. Wördehoff, W. Hoyer, and P. Tamamis. 2016. Uncovering the Binding and Specificity of β-Wrapins for Amyloid-β and α-Synuclein. J Phys Chem B. 120(50):12781-12794.

(18) Orr, A. A., H. Shaykhalishahi, E. A. Mirecka, S. V. R. Jonnalagadda, W. Hoyer, and P. Tamamis. 2018. Elucidating the multi-targeted anti-amyloid activity and enhanced islet amyloid polypeptide binding of β-wrapins. Comput. Chem. Eng. 116(4): 322-332.

(19) Im, W., M. S. Lee, and C. L. Brooks 3rd. 2003. Generalized Born Model with a Simple Smoothing Function. J. Comput. Chem. 24:1691-1702.

(20) Knight, J. L., and C. L. Brooks 3rd. 2011. Surveying implicit solvent models for estimating small molecule absolute hydration free energies. J Comput Chem. 32(13):2909-2923.

(21) Lin, L. N., J. Li, J. F. Brandts, R. M. Weis. 1994. The serine receptor of bacterial chemotaxis exhibits half-site saturation for serine binding. Biochemistry. 33(21):6564-6570.

(22) Iwama, T., I. Kawagishi, S. Gomi, M. Homma, Y. Imae. 1995. In vivo sulfhydryl modification of the ligand-binding site of Tsr, the Escherichia coli serine chemoreceptor. J. Bacteriol. 177(8):2218-2221.